



Dynamic Mechanical and Fracture Behaviour of Sandstone Under Multiaxial Loads Using a Triaxial Hopkinson Bar

K. Liu¹ · Q. B. Zhang¹ · G. Wu¹ · J. C. Li² · J. Zhao¹

Received: 7 April 2018 / Accepted: 5 December 2018 / Published online: 2 January 2019
© Springer-Verlag GmbH Austria, part of Springer Nature 2019

Abstract

Variations in stress conditions of rocks have been observed during blasting for excavation or large-scale seismic events such as an earthquake. A triaxial Hopkinson bar is developed to apply initial pre-stresses achieving various in situ stress conditions, including uniaxial (principal stresses $\sigma_1 > \sigma_2 = \sigma_3 = 0$), biaxial ($\sigma_1 \geq \sigma_2 > \sigma_3 = 0$) and triaxial ($\sigma_1 \geq \sigma_2 \geq \sigma_3 \neq 0$) confinements, and then to determine properties of materials under multiaxial pre-stress states at high strain rate. A series of tests was conducted on sandstone specimens to investigate dynamic responses under multiaxial pre-stress states. A high-speed camera at the frame rate of 200,000 fps with a resolution of 256×256 pixels was used to capture the fracture characteristics rocks under biaxial compression tests. Experiments show that under the same impact velocity, dynamic properties (e.g. dynamic strength, elastic modulus, fracture modes) of sandstone exhibit confinement dependence. Dynamic strength decreases with increasing axial pre-stress σ_1 along the impact direction, while it increases with the increase of lateral pre-stresses σ_2 and σ_3 . The elastic modulus increases with the confinement varying from uniaxial, biaxial to triaxial compression. Rocks are pulverised into powder under uniaxial pre-stress impact, and fragments are ejected from the free face under biaxial compression, while they show slightly damaged or a macroscopic shear fracture under triaxial compression. The 3D imaging of fracture networks in the damaged/fractured specimens was acquired via the X-ray computed tomography system.

Keywords Triaxial Hopkinson bar · Dynamic loading · Triaxial compression · Strain rate · Multiaxial loads

1 Introduction

Rocks are confined to a certain in situ stress environment in the crust and upper mantle of the earth. Field monitoring reveals that typical tectonic stresses are not uniaxial and rarely axisymmetric (McGarr and Gay 1978), the in situ stresses of rocks increase with depth (Hast 1969; Brown and Hoek 1978) and concentrate locally near geological faults (Ahorner 1975; Engelder and Sbar 1984; Chester and Chester 2000; Ferrarini et al. 2015). The in situ stresses are also redistributed locally to a new state called induced stress during excavation (Karl and Richart 1952; Seager 1964; Lee et al. 1976; Read 2004; Cai 2008; Barton and Shen 2017; Li et al. 2017). In addition to the multiaxial stress confinements,

rocks are also frequently subjected to various types of dynamic loads including mechanical vibrations (Huang and Wang 1999), explosions (Zhao et al. 1999), impacts and seismic events (He et al. 2015; Mudau et al. 2016), and they exist in the forms of time histories of particle acceleration, velocity and displacement. An overview of rock dynamics problems and influencing factors in underground engineering design is shown in Fig. 1. Stress states of surrounding rock of an underground cavern are uniaxial at the location A, biaxial at the location B and triaxial at the location C; therefore, rocks are normally under static–dynamic coupling loading conditions (e.g. Li et al. 2008; Xia and Yao 2015; Du et al. 2016; Hokka et al. 2016). Understanding dynamic behaviour of confined rocks is essential in dealing with various rock engineering structures, such as underground storage chambers, reservoirs, slopes, and foundations of dams and bridges, during natural and human-induced dynamic sources such as earthquakes, explosions, and impacts.

To investigate mechanical properties and fracture behaviour of rocks under confinement, quasi-static triaxial compression tests have been widely conducted to determine

✉ Q. B. Zhang
qianbing.zhang@monash.edu

¹ Department of Civil Engineering, Monash University, Melbourne, VIC 3800, Australia

² School of Civil Engineering, Southeast University, 210096 Nanjing, China

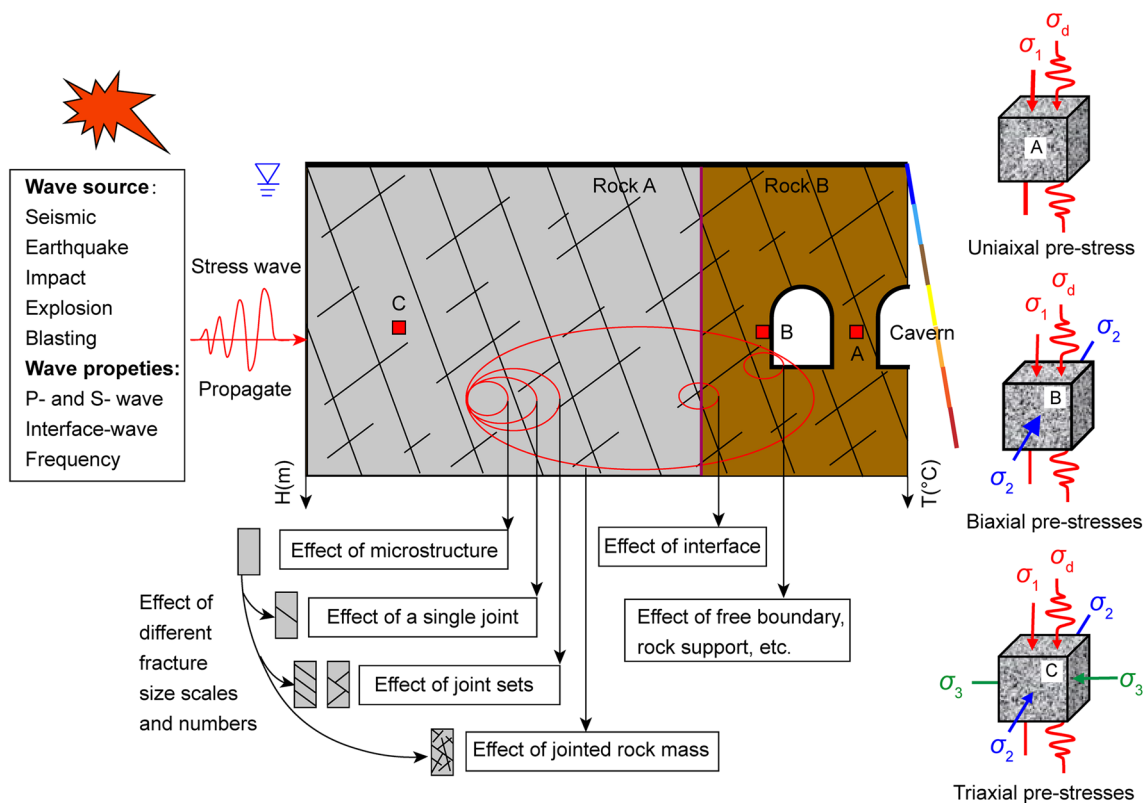


Fig. 1 Overview of rock dynamics problems and influencing factors in underground engineering design (revised after Zhang and Zhao 2014)

the mechanical behaviour of rocks under a controlled set of loading path and stress state (Akers et al. 1986). Mogi (1971) pioneered a true triaxial testing apparatus for precisely testing mechanical behaviour of rocks subjected to three unequal principal stresses ($\sigma_1 \geq \sigma_2 \geq \sigma_3 \neq 0$, where σ_1 , σ_2 , and σ_3 are the maximum, intermediate and minimum principal stresses, respectively), demonstrating that rock strength also depends on the intermediate principal stress σ_2 . After that, several types of true triaxial apparatus have been developed to extensively study the characteristics of rocks under quasi-static true triaxial confinement (Takahashi and Koide 1989; Chang and Haimson 2000; Kwasniewski et al. 2003; Lee and Haimson 2011; Descamps et al. 2012; Ingraham et al. 2013; Schwartzkopff et al. 2013). Testing results from triaxial compression reveal that stress condition affects rock properties including strength, deformation and failure modes (Jaeger et al. 2009; Kwaśniewski 2012). There exist general trends for: an increase of triaxial strength with increasing intermediate principal stress σ_2 at a given σ_3 ; the ductility of deformation behaviour increases with an increase of σ_3 , but decreases when σ_2 is increased; and the fracture planes of rock are parallel to the direction of σ_2 , and the fracture angle (the angle between the direction of σ_1 and the fracture plane) decreases with increasing σ_2 , especially at low minimum stresses. It should be noted that,

rocks failures in these triaxial compression tests are at a low strain rate ($< 10^{-1}/s$) due to the hydraulic limitation of true triaxial apparatus (Zhang and Zhao 2014). Thus, more intricate studies of rocks under multiaxial confining stress states are required at high strain-rate levels consistent with those prevailing in explosion, blasting, impact and earthquake.

The split Hopkinson pressure bar (SHPB) (Hopkinson 1914) or Kolsky bar (Kolsky 1949) has been widely used for the determination of dynamic properties of rock materials at high strain rates (e.g. Green and Perkins 1968; Kumar 1968; Perkins et al. 1970; Frew et al. 2001; Li et al. 2005; Xia et al. 2008; Dai et al. 2010; Chen and Song 2010; Zhou et al. 2010; Cadoni 2010; Zhang and Zhao 2013; Xing et al. 2018a, b), and it is shown that the strain rate has a significant effect on rock strength (Zhang and Zhao 2014; Liu et al. 2018). However, the strain rate dependence of mechanical properties may be different under various confining pressures (Paterson and Wong 2005; Zhang and Zhao 2014). Over the past decades, the SHPB has also been modified to apply confinements on brittle materials such as rocks (Christensen et al. 1972; Lindholm et al. 1972, 1974; Li et al. 2008; Frew et al. 2010), ceramics (Chen and Ravichandran 1996a, 1997) and concrete (Malvern and Jenkins 1990; Gary and Bailly 1998) before dynamic loading. In general, there are two types of approaches to

achieve multiaxial loadings on the specimen in modified SHPB tests, through either pressure or displacement boundary condition (Chen and Song 2010; Zhang and Zhao 2014). The pressure boundary condition is achieved through hydrostatic pressure by a hydraulic confining chamber. In the early 1970s, Lindholm and his colleagues developed this modified SHPB system with two hydraulic cylinders, allowing for axial preloading, radial confining pressure and high strain rate (up to $10^3/s$) loadings required for the testing of Dresser basalt (Lindholm et al. 1972, 1974). This design was further improved and employed to study the dynamic properties of specimens under confining pressure (e.g. Lankford 1976, 1994; Kawakita 1981; Wang and Yu 1992; Li et al. 2008; Paliwal et al. 2008; Kabir and Chen 2009; Frew et al. 2010; Wang and Liu 2011; Lindholm 2012; Yin et al. 2012; Farbaniec et al. 2017). The confinement in the SHPB can also be achieved by using the displacement boundary condition, in which either a shrink-fit metal sleeve or a passive thick vessel is employed to jacket the cylindrical surface of the specimen. Malvern et al. firstly employed passive confining jacket system to impose controlled lateral confinement on the cylindrical rock-like specimen (Malvern and Ross 1986; Gong and Malvern 1990; Malvern and Jenkins 1990). This method was further performed to study dynamic properties of solid materials (e.g. Albertini and Montagnani 1994; Chen and Ravichandran 1996b, 1997; Nemat-Nasser et al. 2000; Rome et al. 2000; Forquin et al. 2008; Bailly et al. 2011; Yuan et al. 2011; Martin et al. 2013; Hokka et al. 2016). In addition, some other modified SHPB integrated with a hydraulic system have also been developed to investigate dynamic tensile behaviour (e.g. tensile strength, fracture toughness and crack pattern) of rocks under pre-tension (Zhou et al. 2014; Wu et al. 2015; Chen et al. 2016) and hydrostatic confinement conditions (Wu et al. 2016). The dynamic behaviours of rocks under confinement exhibit as followed: triaxial strength increases with the increase of strain rate under all confining pressures; an increase of triaxial strength with increasing confining pressure, as confirmed in quasi-static triaxial tests; the deformation behaviour becomes more ductile at high strain rates; dynamic tensile strength decrease with increasing pre-tension stress, while the total strength (the sum of static pre-tension stress dynamic tensile strength) is independent of pre-tension stress; as the static pre-load increases, the dynamic fracture toughness decreases but total fracture toughness increases. It should be pointed out that, confining pre-stress applied on the specimen in existing SHPB is a still conventional triaxial stress state ($\sigma_1 > \sigma_2 = \sigma_3 \neq 0$), rather than a true triaxial stress state ($\sigma_1 > \sigma_2 > \sigma_3 \neq 0$) before dynamic loading. Until now, there are still missing experimental data on the dynamic properties of rock under true triaxial confining stresses at high strain rates ($> 10/s$), which is highly required in rock engineering design.

Great efforts have been made to achieve an initial triaxial quasi-static pressure before the specimen undergoes dynamic loading since 2009, as stated by Albertini (2013) ‘*The 3D-Modified Hopkinson Bar has been substantially conceived through discussions among Carlo Albertini, Prof. Ezio Cadoni and Prof. Jian Zhao*’. The proposed 3D-MHB apparatus consists of one hydraulic actuator connected to the pre-tensioned bar, and of five other hydraulic actuators installed at the end of the five output bars (Cadoni and Albertini 2011). The quasi-static triaxial stress state on a specimen is introduced by the hydraulic actuators of the output confinement bars. The dynamic loads are generated by the rupture of the brittle bolt into the system. However, the 3D-MHB apparatus has only achieved the uniaxial function but no lateral confinement (Zhao and Cadoni 2011; Cadoni et al. 2015). With the support of Australian Research Council (ARC) (Zhao et al. 2015), a triaxial Hopkinson bar has been developed and installed at Monash University, which allows for investigating dynamic mechanical and fracture behaviour of geomaterials under multiaxial confinements. The major differences between the triaxial Hopkinson bar and 3D-MHB are: the triaxial prestresses are achieved by three pairs of hydraulic cylinders and wedge reaction devices installed on the ends of the six square bars, and the gas gun launches a cylindrical striker to generate dynamic loads. The applications of triaxial Hopkinson bar have been verified by multiaxial compression, tension and shear tests.

This study investigates dynamic behaviours of rocks under various confinement conditions, including uniaxial, biaxial and triaxial confinements. Sandstone specimens are subjected to various quasi-static confining pressures before dynamic loading with the same impact velocity. Experimental results on the confinement dependence of dynamic mechanical properties of sandstone are presented and discussed in detail. We examine the confinement dependence of compressive strength, strain to failure, elastic modulus, and failure modes at high strain rates. The real-time fracturing process of rock specimen during impact is digitally captured using the high-speed photography, and the internal fracture pattern of rock under triaxial compression is detected by the micro-CT (μ CT) technique. The roles of time and pre-stress in the processes of rock fracture can be elucidated, which provides an improved understanding of the dynamic behaviour of rocks under a wide range of stress conditions.

2 Experimental Procedures

2.1 Specimen Preparation

Sandstone specimens were extracted from the same rock block without visible geological discontinuities in Sichuan, China. Petrographic studies were performed to probe an

insight of the mineralogical composition and grain sizes, standard thin sections analysed under cross-polarised transmitted light with different magnifications are shown in Fig. 2. Sandstone comprises quartz (30%), feldspar (20%), other minerals (20%) and matrix (30%), and the range of mineral size is from 200 to 500 μm with average quartz size of 350 μm . The quartz and feldspar consist of irregularly shaped fragments that seem to form the framework. In addition, the darker domains of very fine-grained mud and clay minerals fill up space.

The prepared sandstone specimens have the following physicomaterial properties: density $\rho = 2350 \text{ kg/m}^3$, P -wave velocity $C_L = 2600 \text{ m/s}$, elastic modulus $E = 9.50 \text{ GPa}$, Poisson's ratio $\nu = 0.21$, and uniaxial compressive strength (UCS) $\sigma_c = 40 \text{ MPa}$. The standard cubic specimens are $50 \times 50 \times 50 \text{ mm}^3$ with elaborate preparation, the size of the specimen should be at least ten times the average grain size in the rock (Zhou et al. 2012). These specimens are polished to a tolerance of 0.05 mm across the face of $50 \times 50 \text{ mm}^2$, and the accuracy of the specimen size is kept within $\pm 1\%$. The parallelism of these three opposite pairs of faces is less than 0.05 mm in 50 mm. The adjacent surfaces of the cubic specimen have a good perpendicularity with the maximum deviation of less than 0.25° .

2.2 Triaxial Hopkinson Bar System

Experimental tests for dynamic uniaxial, biaxial and triaxial strength of rocks were conducted using a triaxial Hopkinson bar system at Monash University, as shown in Fig. 3. It consists of a dynamic loading system including a gas gun and a cylindrical striker bar (42CrMo Steel, $\rho = 7850 \text{ kg/m}^3$, $E = 210 \text{ GPa}$, $C_s = 5200 \text{ m/s}$, $\sigma_p = 930 \text{ MPa}$, $L = 0.5 \text{ m}$, $\Phi 40 \text{ mm}$, impact velocity up to 50 m/s), three independent pairs of steel square bars (42CrMo Steel, cross-section $50 \times 50 \text{ mm}^2$) in three perpendicular directions, three hydraulic cylinders (pressure capacity up to 100 MPa), a strong platform, six pieces of high-strength steel reaction frame, and a multi-channel high-speed data acquisition system. The square bars are aligned orthogonally in X , Y and Z

directions. Along with X axial direction, there is a dynamic loading system of the gas gun with a striker barrel (1.5 m), an incident bar (2.5 m), a transmission bar (2 m), an absorption bar (0.5 m), a hydraulic load cylinder and a moment-trap device. In Y and Z axial directions, four steel output bars (2 m) are used to apply confining pressure by hydraulic load cylinders and to monitor the output waves. Altogether, the total size of the apparatus is 8 m length in the horizontal X direction, 5 m width in the horizontal Y direction and 5 m height in the vertical Z direction. During the experiment, the pre-stresses can be applied in three independent orthogonal directions on a cubic specimen by two horizontal hydraulic cylinders and one vertical hydraulic cylinder, and the dynamic loads can be applied by launching a striker bar in the gas gun. The triaxial static–dynamic coupled loading can be achieved, allowing the investigation of the influence of the triaxial quasi-static pre-stress on the dynamic behaviour of rocks.

To visualise the stress wave propagation in the square bar (cross-section $50 \times 50 \text{ mm}^2$) impacted by a cylindrical striker (diameter 40 mm), numerical modelling (ABAQUS software, version 6.14-1) is conducted. Figure 3c shows stress wave propagation in the square bar without a pulse shaper under the impact velocity of 20 m/s. Inevitably, the deformation of the impact surface of the incident bar is non-uniform due to the mismatch of the contact area between the cylindrical striker and the square bar. Several monitoring points (A, B, C and D) in the square bar are selected to measure the incident wave. Although the oscillations of incident stress waves are observed due to a lack of the pulse shaper, both the amplitude and duration of stress waves are well consistent with each other, which indicates that the front of the incident wave is flat with the error of less than 3%. In other words, the stress equilibrium is well achieved in the cross section of the square bar, though there is a certain degree of local stress concentration at the corners. Therefore, strain gauges mounted on the surfaces of the bars can accurately capture the signals during the dynamic triaxial compression tests.

Fig. 2 Thin sections of sandstone with different magnifications under cross-polarised micrographs

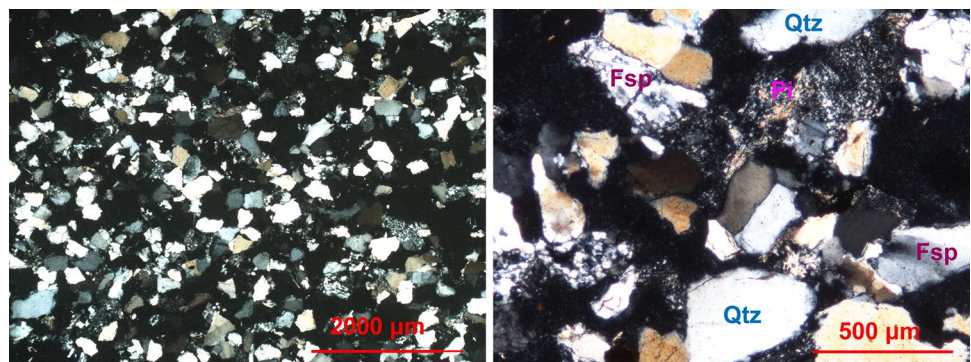
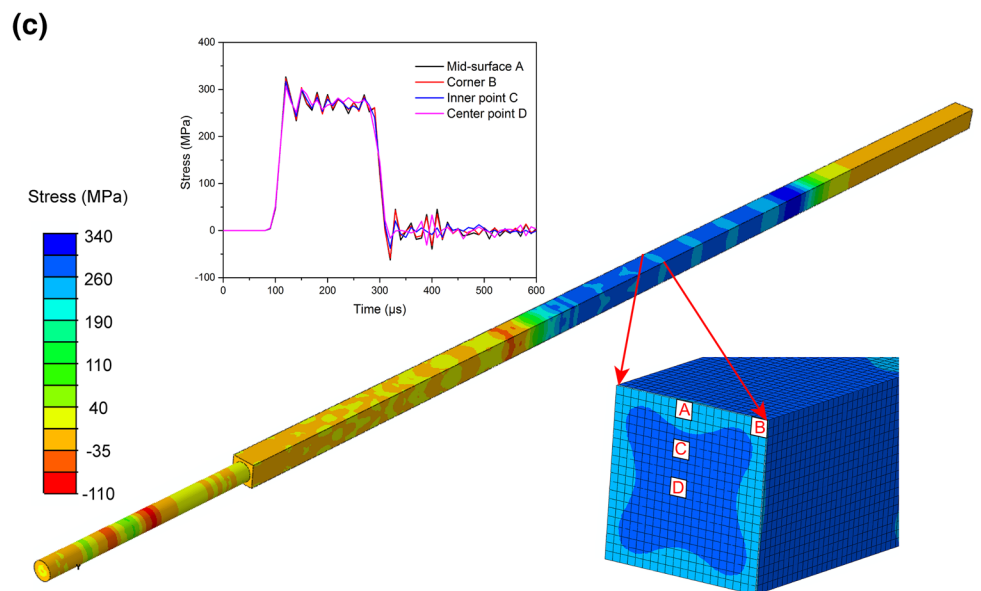
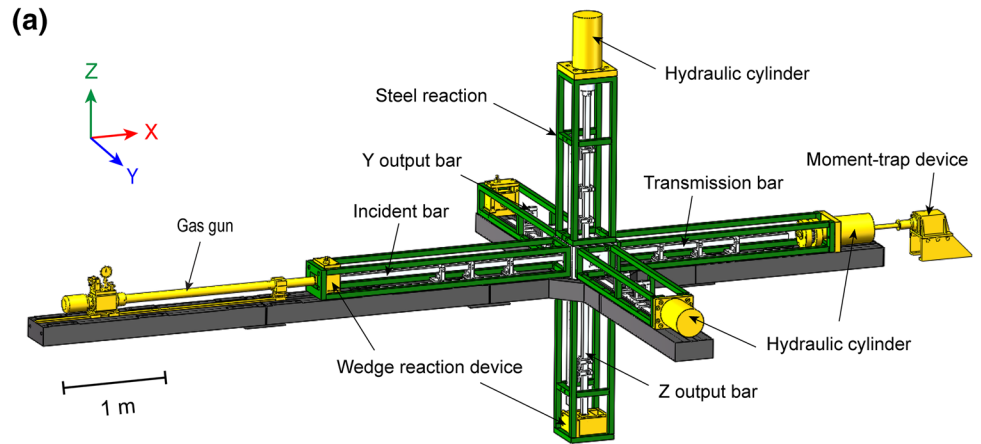


Fig. 3 Schematic (a) and photo (b) of the triaxial Hopkinson bar (X-axis refers to impact direction), and c numerical modelling stress wave propagation in the square bar impacted by a cylindrical striker



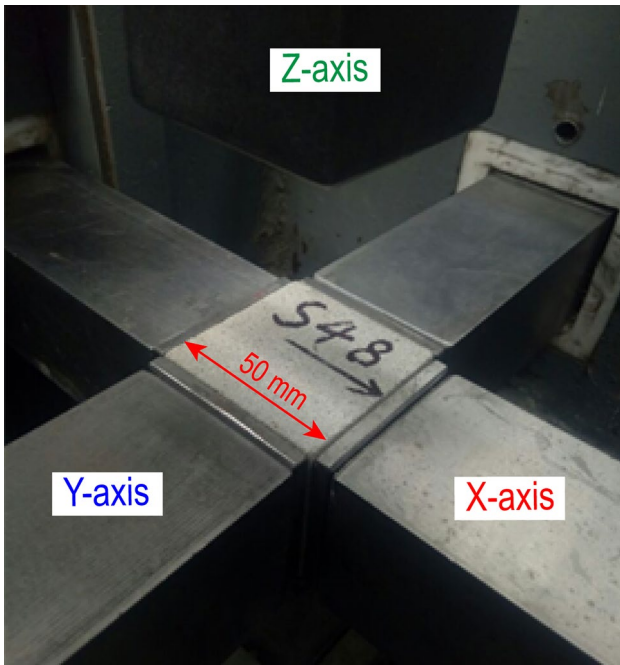


Fig. 4 Standard cubic rock specimen placed between bars in the loading cell

During the test, the specimen (Fig. 4) is placed in the loading cell, which is right at the intersection point of the axis of six bars. Firstly, the specimen is subjected to a desired multiaxial pre-stress condition by the hydraulic cylinders; then dynamic loading is applied from the impact of the striker bar on the front end of the incident bar. The generated incident pulse propagates along the incident bar and impacts on the testing specimen until failure, leading to the reflected wave and transmission wave as well as output waves in Y/Z directions.

Six sets of strain gauges (FLA-6-11) were attached on the incident bar, transmission bar in X direction and four output bars in Y and Z directions, respectively. Each set consists of two strain gauges located diametrically opposite. The testing signals are recorded by a 12-bit analogue-to-digital converter (NI PXIe-5105) with a high sampling rate (1 MS/s) connected to strain gauges through Wheatstone bridges and a differential amplifier (SDY-2107A dynamic strain meter). Red copper discs with the dimension of 15 × 1.5 mm (diameter × thickness) are served as pulse shapers, which can produce a well-repeatability ramped incident wave that reduces high-frequency oscillations and minimises the dispersion effect. The interfaces between the bars and test specimen are lubricated by petrolatum to minimise the friction. The velocity of the striker bar is measured by a laser-beam velocity measurement system (HPCSY-II) before impacting on the incident bar. When the striker bar moves in the moment before impact, the parallel light curtain generated

by a transmitter is blocked progressively. Once the change of light intensity is detected by the receiver, an analogue voltage signal in a function of time is emitted and recorded by the digital storage oscilloscope.

In the triaxial Hopkinson bar experiment, as shown schematically in Fig. 5, the stress wave propagates through the incident bar, rock specimen, transmission/output bars and deform the specimen at high strain rate until failure. Along the impact direction, the elastic one-dimensional (1D) stress wave propagation theory is used to interpret signals obtained in triaxial Hopkinson bar tests. Thus the dynamic forces $P_1(t)$ and $P_2(t)$ and the velocities $V_1(t)$ and $V_2(t)$ acting on the bar-specimen interfaces along the X direction can be calculated by (Kolsky 1949, 1953):

$$P_1(t) = A_b E_b [\epsilon_{in}(t) + \epsilon_{re}(t)], \quad P_2(t) = A_b E_b \epsilon_{tr}(t), \quad (1)$$

$$V_1(t) = C_b [\epsilon_{in}(t) - \epsilon_{re}(t)], \quad V_2(t) = C_b \epsilon_{tr}(t), \quad (2)$$

where E_b is Young’s modulus of bars; A_b is the cross-sectional area of the bar; C_b is the longitudinal wave velocity of the bars; ϵ is the strain measured by strain gauges on the bars. The subscripts ‘in’, ‘re’ and ‘tr’ correspond to the incident, reflected and transmission waves in the impact direction, respectively.

Assuming the stress equilibrium or uniform deformation prevails in the specimen during the dynamic loading (i.e. $\epsilon_{inx}(t) + \epsilon_{rex}(t) = \epsilon_{trx}(t)$), the average stress σ , strain ϵ and strain rate $\dot{\epsilon}$ of the specimen can be determined with the equations:

$$\sigma_x(t) = \frac{P_1(t) + P_2(t)}{2A_s} = \frac{E_b A_b}{2A_s} [\epsilon_{in}(t) + \epsilon_{re}(t) + \epsilon_{tr}(t)] = \frac{E_b A_b}{A_s} \epsilon_{tr}(t), \quad (3)$$

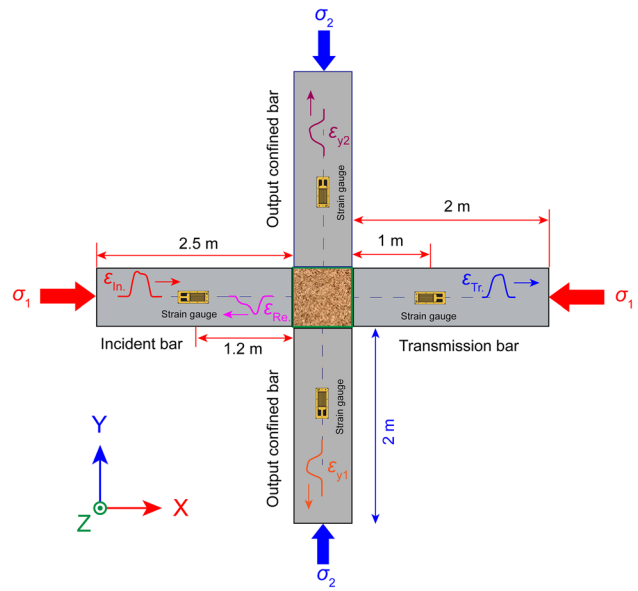


Fig. 5 Schematic of stress waves propagation in the triaxial Hopkinson bar (not to scale, top view from vertical Z direction)

$$\dot{\epsilon}(t) = \frac{V_1(t) - V_2(t)}{L} = \frac{C_b}{L} [\epsilon_{in}(t) - \epsilon_{re}(t) - \epsilon_{tr}(t)] = -\frac{2C_b}{L} \epsilon_{re}(t), \tag{4}$$

$$\begin{aligned} \epsilon(t) &= \int_0^T \dot{\epsilon}(t) dt = \frac{C_b}{L} \int_0^T [\epsilon_{in}(t) - \epsilon_{re}(t) - \epsilon_{tr}(t)] dt \\ &= -\frac{2C_b}{L} \int_0^T \epsilon_{re}(t) dt, \end{aligned} \tag{5}$$

where A_s is the cross-sectional area and L is the length of the specimen.

The respective stress and strain of the specimen in the Y and Z directions can be calculated by (Cadoni and Albertini 2011):

$$\sigma_y(t) = \frac{E_b A_b}{2A_s} [\epsilon_{y1}(t) + \epsilon_{y2}(t)], \tag{6}$$

$$\epsilon_y(t) = \frac{C_b}{L} \int_0^T [\epsilon_{y1}(t) + \epsilon_{y2}(t)] dt, \tag{7}$$

$$\sigma_z(t) = \frac{E_b A_b}{2A_s} [\epsilon_{z1}(t) + \epsilon_{z2}(t)], \tag{8}$$

$$\epsilon_z(t) = \frac{C_b}{L} \int_0^T [\epsilon_{z1}(t) + \epsilon_{z2}(t)] dt, \tag{9}$$

where $\sigma_y(t)$ and $\sigma_z(t)$, $\epsilon_y(t)$ and $\epsilon_z(t)$ are the stress and strain of specimen along the Y and Z directions, respectively. Thus the dynamic behaviour of geomaterials (e.g. rocks, coal, concrete, mortar and ceramics) under different stress states can be quantitatively determined.

2.3 Loading Paths and Experimental Procedures

In general, the multiaxial confining loadings can be classified into uniaxial ($\sigma_1 > \sigma_2 = \sigma_3 = 0$), biaxial ($\sigma_1 > \sigma_2 \neq 0$, and $\sigma_3 = 0$) and triaxial ($\sigma_1 > \sigma_2 > \sigma_3 \neq 0$) pre-stress conditions. In this study, the dynamic confinement tests on sandstone specimens with different pre-stress states (e.g. uniaxial, biaxial and triaxial compression pre-stresses) are carried out under the same impact velocity of 20 m/s. During the dynamic true triaxial test, the stress path is schematically shown in Fig. 6, the specimen is subjected to the desired stress state such as $\sigma_1 > \sigma_2 > \sigma_3$ with a low loading rate of $\sim 10^{-4}$ GPa/s, and then a dynamic loading is applied along the σ_1 direction until rock failure.

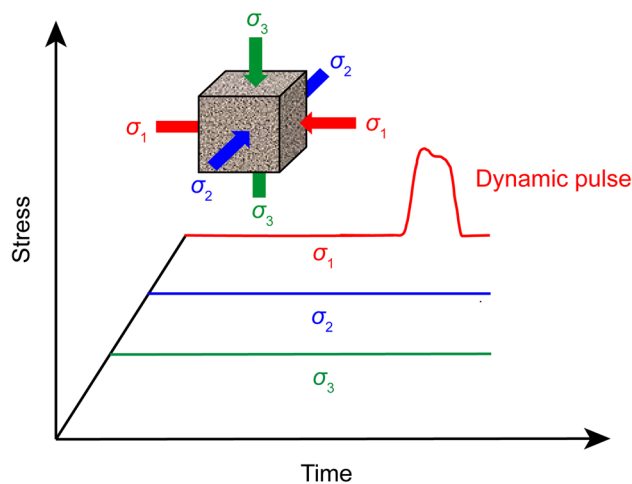


Fig. 6 Loading paths of experimental testing in this study

2.4 Data Interpretation

Since all of the pre-stresses and impacts are compressive, the compression is defined as positive in this study. The typical signals obtained in the impact direction of a dynamic triaxial test with the pre-stress state of (30, 20, 10) MPa are shown in Fig. 7a. For axially confined SHPB, when the striker bar impacts the incident bar, the wedge reaction device unloads and the axial pre-stress subsequently relaxes. Therefore, the stress in the incident bar becomes tensile after the incident pulse when the axial compressive pre-stress in the bar unloads. The stress value (30.29 MPa) of the baseline of reflected wave indicates the level of applied axial pre-stress σ_1 (30 MPa) in the X direction. To avoid the superposition of tensile pulse induced by the unloading interaction of wedge fix device and the incident bar, appropriate positions of strain gauges on the incident bar are carefully checked to obtain distinct incident and reflected signals. In the interpretation of signals, it is necessary to subtract the pre-stress from the reflected wave before calculating the strain rate and dynamic strain of the specimen (Hokka et al. 2016). The transmission bar does not receive the unloading pulse from wedge reaction device until the experiment is complete (Frew et al. 2010).

Figure 7b shows that during the impact in the X direction, the generated stress waves propagate along the Y and Z bars owing to the Poisson effect of rock specimen, which results in the variations of confinement in Y and Z directions. These signals provide not only the deformation information of the specimen, but also contain energy release during material fracturing. The difference of peaks values of signals obtained in Y and Z bars is related to the pre-stresses and the fracture behaviour (e.g. direction, length and number of fractures and fracture energy) of rock. Figure 7c shows the evolution of three principal

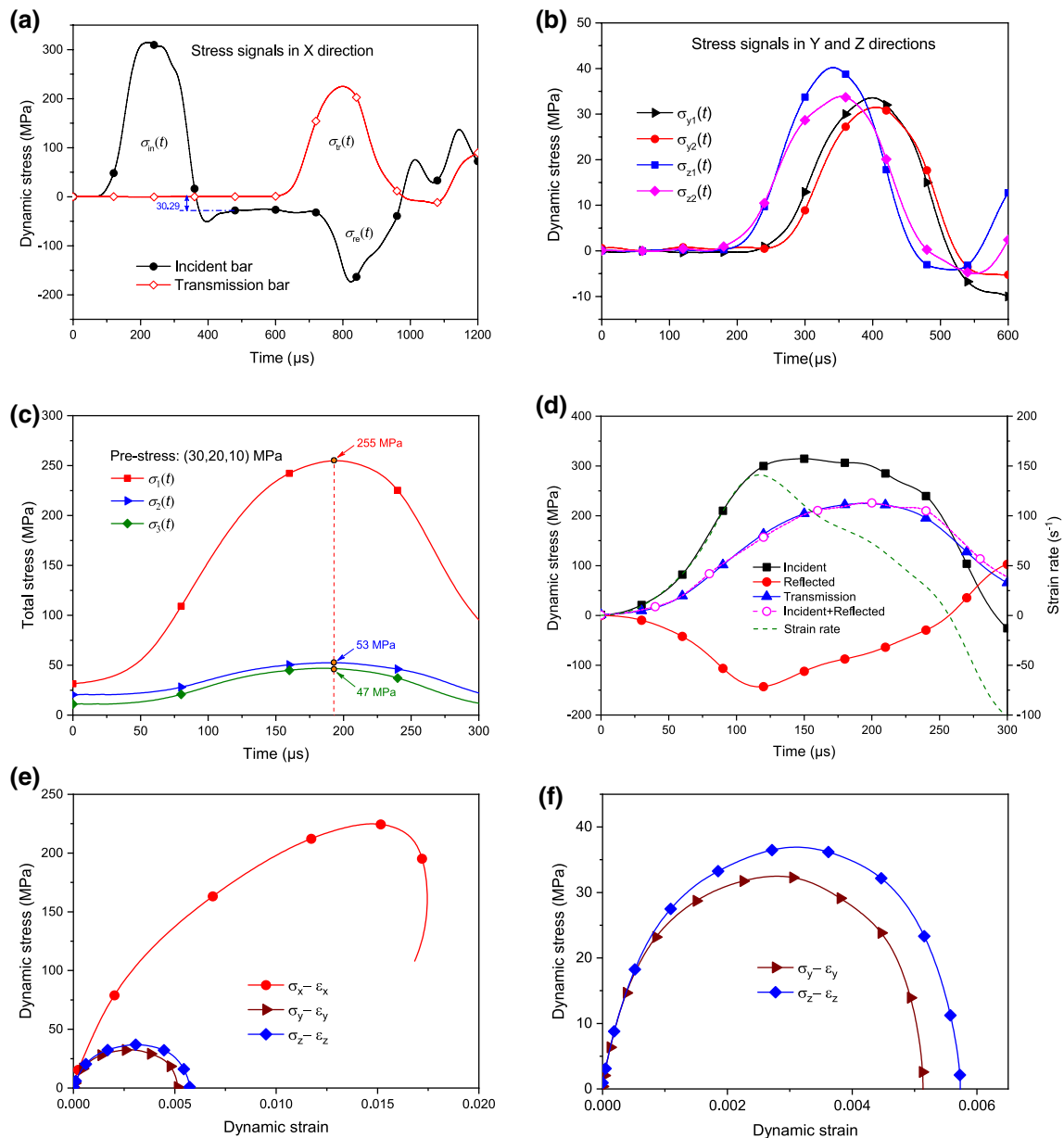


Fig. 7 Typical experimental data at the impact velocity of 20 m/s and pre-stress conditions (30, 20, 10) MPa: **a** stress waves in impact direction; **b** stress waves in Y/Z direction; **c** dynamic stress evolution

applied on the specimen; **d** dynamic stress equilibrium check; **e** stress and strain history in three directions; **f** stress and strain history in Y/Z directions

stresses (σ_1 , σ_2 and σ_3) acting on the rock specimen during impact, which include both static pre-stresses and dynamic stresses. The three principal stresses initiate from (30, 20, 10) MPa and then rise to the peak point (255, 53, 47) MPa at the moment of rock breakage. Although the total bearing capacity (i.e. the sum of pre-stress and dynamic strength) of materials might be significant for the materials under certain conditions, for rock materials under the in situ conditions (internal quasi-static loading), the dynamic strength is only be considered after the influence

of external dynamic sources. It should be pointed out that the stresses of the peak point (i.e. confined stresses at rock failure) are the most important values which can be used to calibrate dynamic constitutive models. However, it is not possible to control and obtain the same desired peak stresses within a transient state of any dynamic experiment. Given the initial pre-stresses are closely related to the peak stresses and easy to control in the dynamic experiment, the relationship between pre-stresses and dynamic strength of rocks is presented in the following sections.

For a valid SHPB test, dynamic stresses associated with axial and radial inertia should be substantially small compared with the flow stress of the material under investigation. Under stress equilibrium, the stress gradient vanishes, and inertial effects induced by stress wave propagation can thus be minimised. The red copper sheet used as the pulse shaper lengthens the rise time of the incident stress wave facilitating the stress of specimen to equilibrate during the time of interest for the test. In axial confined SHPB, the axial pre-stress in the impact direction has been verified to affect the stress equilibrium of dynamic experiments (Kabir and Chen 2009; Hokka et al. 2016; Chen et al. 2017). Thus the stress equilibrium condition in axially constrained SHPB tests requires careful examination. Figure 7d presents the dynamic stress balance check between both ends of the specimen along the X direction in the triaxial Hopkinson bar tests. It is observed that the uniformity of the dynamic stress across the specimen is well achieved in the axial impact direction, and thus the axial inertial effect is reduced to a negligible level. Although there exists inevitably dynamic friction at the interfaces between rock specimen and lateral output bars, the achieved dynamic stress balance also demonstrates that 1D stress wave propagation theory can be employed to calculate the stress–strain history of rock specimen in triaxial Hopkinson bar tests. According to Eqs. (3–9), the obtained stress and strain history curves in three directions are shown in Fig. 7e, f.

2.5 High-Speed Imaging and Micro-CT (μ CT) Reconstruction

The high-speed imaging technique is capable of visualising the real-time deformation and fracturing process of the specimen in dynamic experiments (Xing et al. 2017). To study the deformation characteristics and fracture patterns of rocks under dynamic biaxial compression tests, a high-speed CMOS camera (Phantom V2511) was adopted with the resolution of 256×256 pixels and the frame rate of 200,000 fps. With the lens of Nikon AF-S DX Nikkor 18–105 mm F/3.5–5.6 G ED, the high-speed camera was mounted on the tripod and preheated for 40 min to achieve the stable working environment. During the impact, the camera was triggered by two synchronous transistor–transistor logic (TTL) signals, which were generated by a digital trigger provider (NI BNC-2090A) when the striker passed the laser beam. Two 84 W LED lights (GS Vitec MultiLED LT) provided 15,400 Lumen in total for the illumination.

X-ray computed tomography or micro-CT (μ CT) has been a frequently used non-destructive 3D imaging and analysis technique for the investigation of internal structures of a large variety of objects, including geomaterials like soils, rocks, concrete and fossils (Cnudde and Boone 2013). For rock specimens after triaxial compression, this technique

was adopted to identify and reconstruct the 3D micro-cracks inside the recovered rock specimen. The damaged specimen was scanned using a Zeiss Xradia 520 Versa for imaging geomaterials available at Monash University (Al Mahbub and Haque 2016), which provides non-destructive 3D imaging of fracture networks induced by the impact. Sandstone specimen was digitally scanned with a resolution spatial resolution of $50 \times 50 \times 50 \mu\text{m}^3$, an electron current of $72 \mu\text{A}$ and an accelerating voltage of 140 keV. All micro-CT images obtained were processed and analysed using Avizo 9.5 software developed by FEI Visualisation Sciences Group.

3 Dynamic Behaviours of Rocks Under Multiaxial Pre-stress Loads

3.1 Effect of Uniaxial Pre-stress

To investigate the effect of initial axial pre-stress on dynamic properties of rocks, a series of dynamic uniaxial tests is conducted. According to the static uniaxial compressive strength (UCS) (40 MPa) of the sandstone, the applied axial pre-stress are 10, 20 and 30 MPa, which are 25%, 50% and 75% of the static UCS, respectively. The impact velocity of the striker bar is 20 m/s, which can induce an impact pulse with an amplitude up to 315 MPa.

Figure 8 shows the dynamic stress–strain curves of sandstone subjected to the same impact velocity but different axial pre-stress. The axial strain in the X direction was measured by the strain gauges and can be determined by integrating Eq. (4), whereas the stress was calculated from the transmission bar signals using Eq. (3). The strain gauge bridges were rebalanced after the quasi-static loading of the specimen.

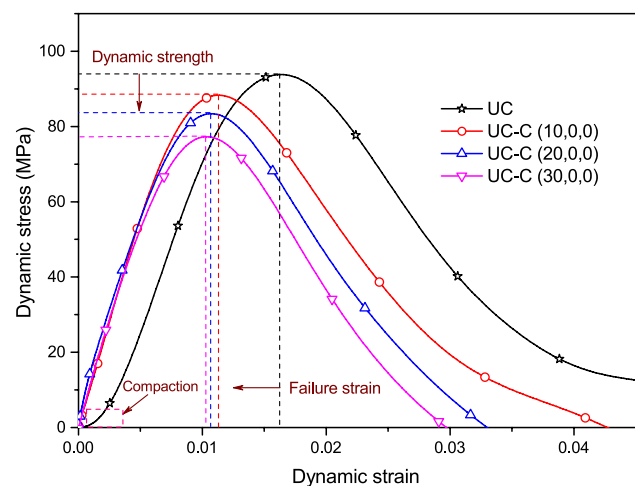


Fig. 8 Stress–strain curves of sandstone at the impact velocity of 20 m/s under different axial pre-stresses in dynamic uniaxial tests (UC uniaxial compression, UC-C confined UC)

Therefore, the integrated strain is the dynamic strain instead of the total axial strain because it does not include the shortening of the specimen due to the application of axial pre-stress. The dynamic deformation behaviour of rock specimens with axial confinement was significantly different from that of unconfined ones. The dynamic stress–strain curve of the axial unconfined specimen has four stages, i.e. compaction, elastic deformation, accumulative damage and complete failure, which is typical for sandstone under conventional uniaxial compressive loading. With axial pre-stress, however, there is no compaction stage in the initial part of the dynamic stress–strain curves of sandstone, which comprise a linear elastic part followed by nonlinear deformation and peak stress. The post-peak behaviour of axial unconfined and confined sandstone shows a similar trend. The strength of sandstone declines rapidly after the primary fracture, and followed by further compaction of the fractured pieces.

At the impact velocity of 20 m/s, the average value of dynamic uniaxial strength of the unconfined sandstone is 93 MPa, which is 2.3 times of the quasi-static UCS of 40 MPa, proven that sandstone has rate-dependent behaviour. Furthermore, it can be found that the axial pre-stress also affects the dynamic responses of sandstone, which is in line with those of previous studies (Li et al. 2008, 2009). In the dynamic uniaxial test, the dynamic compressive strength σ_d of sandstone decreases linearly with increasing axial pre-stress, as shown in Fig. 9a. When the pre-stresses increase from 25 to 75% of the quasi-static UCS, the dynamic UCS of sandstone decreases by 17% from 93 to 77 MPa, with a linear trend. Moreover, the failure strain (the strain necessary to failure) is also related to axial pre-stress. Failure strain decreases by nearly 16.7% from 0.012 to 0.01 with the increase of the axial pre-stress, which indicates that the energy necessary to dynamically break the rock is lower at higher axial pre-stress.

The reduction of dynamic strength is related to the damage initiation induced by the applied axial pre-stress. When an axial pre-stress is applied, the pre-existing micro-cracks tend to be closed and rock specimen deforms elastically without damage. For the micro-cracks with directions perpendicular to the pre-stress, the initiation and propagation of cracks can be easily induced by reflected tensile stress at the crack surface. If these micro-cracks are compacted by the pre-stress, the stress wave can smoothly propagate across these cracks without reflecting tensile stress, and thus the crack propagation can be suppressed. In this regard, the dynamic strength of rock may increase with the increasing of axial pre-stress. However, this phenomenon cannot be observed in our experiments because of the low porosity and good integrity of fine sandstone. With the uniaxial pre-stress increases from 10 to 30 MPa near or over the UCS of sandstone, a large number of pre-existing micro-cracks inside specimens are reactivated before impact, leading to damage of the rock and thus its dynamic strength decrease rapidly.

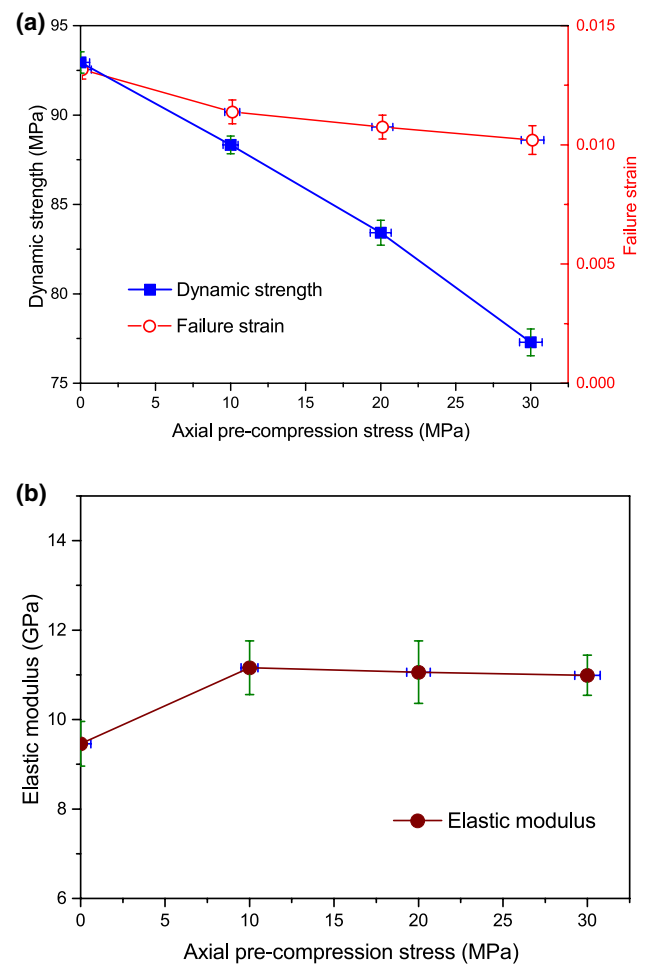


Fig. 9 Effects of axial pre-stress on **a** peak strength, failure strain and **b** elastic modulus of sandstone specimens at the impact velocity of 20 m/s

Elastic modulus commonly describes the macroscopic response of the internal microstructure to the external load. The elastic modulus in the dynamic test is determined by the slope of the linear segment of a dynamic stress–strain curve. Figure 9b shows the relation between the elastic modulus and initial axial pre-stress. It can be observed that the elastic modulus seems to be insensitive to the variation of axial pre-stress. The average elastic modulus is around 11 GPa, which is close to the value obtained from the quasi-static UC test.

The failure observation of dynamically loaded specimens with different axial pre-stresses is shown in Fig. 10. When the pre-stress is 10 MPa, the sandstone specimens are completely broken into small fragments (Fig. 10a) at the impact velocity of 13 m/s. However, the sandstones are pulverised severely into powder (Fig. 10b, c) at a high impact velocity of 20 m/s under different axial pre-stresses, owing to the high impact velocity or loading rates. A similar phenomenon has been reported and

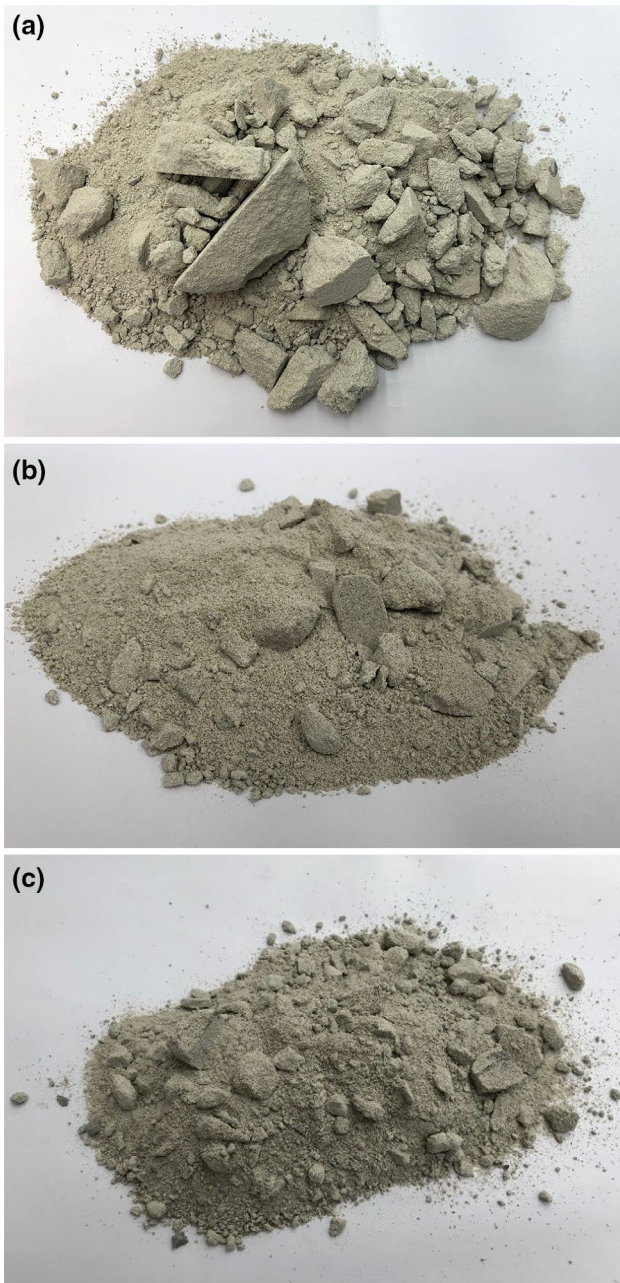


Fig. 10 Fractured sandstone specimens after the impact with different axial pre-stresses: **a** 10 MPa ($v=13$ m/s); **b** 10 MPa ($v=20$ m/s); **c** 30 MPa ($v=20$ m/s)

interpreted in the previous publications (Olsson 1991; Li et al. 2005; Cai et al. 2007; Doan and Gary 2009).

3.2 Effect of Biaxial Pre-stress

In the biaxial pre-stress tests, the pre-stresses σ_1 and σ_2 are applied along X direction and Y direction, respectively, while

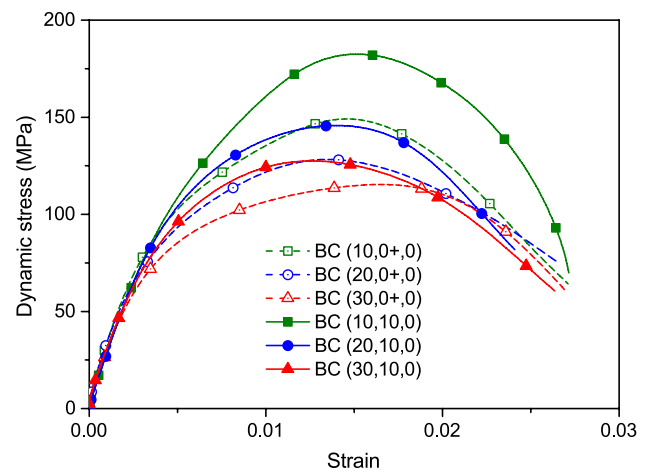


Fig. 11 Effects of axial pre-stress σ_1 on dynamic stress–strain curve of sandstone under biaxial compression at the impact velocity of 20 m/s (BC biaxial compression)

σ_3 is constant at 0 along Z direction during the test. The dynamic loadings are applied along the direction of major principal stress σ_1 . It is important to note that, when the initial σ_2 is marked as 0+, it refers to the case that the surfaces of the bar and rock specimen are contacted with each other but without any pre-stress applied before impact, thus the dynamic evolution of confining stress σ_2 can still be captured on the Y bars due to the Poisson effect of materials and inertial effect of the bar.

During the tests, sandstone fails under dynamic loading at the impact velocity of 20 m/s with an average strain rate of 165/s, and a large number of fragments were rapidly ejected from the free face in the Z direction. The dynamic stress–strain curves of sandstone at the impact velocity of 20 m/s can be obtained with various biaxial pre-stress states. It is first observed that both σ_1 and σ_2 affect the dynamic strength of sandstone under biaxial pre-stress compression. It can be found in Fig. 11, in dynamic biaxial tests under the pre-stress states varying from (10, 0+, 0) to (30, 0+, 0) MPa with increasing σ_1 , the failure strength of sandstone decreases with increasing the axial pre-stress, a similar trend can also be found when the pre-stress states change from (10, 10, 0) to (30, 10, 0) MPa. During the impact, the maximum principal stress is always along the impact direction. An increasing pre-stress σ_1 leads to the activation of the opening of micro-cracks which are along the impact direction before impact, and this initial damage results in a reduction of dynamic strength of rock under biaxial compression loads. However, the dynamic strength of sandstone raises as the lateral pre-stress σ_2 increases from 0 to 20 MPa when the initial σ_1 is 20 MPa (Fig. 12a). At the higher initial σ_1 of 30 MPa, as shown in Fig. 12b, the dynamic strength also increases with the increase of σ_2 from 0 to 30 MPa. Besides, the stress–strain curves show that sandstone

deforms elastically at the initial stage without compaction and behaves nonlinearly until failure.

More details on the effects of σ_1 and σ_2 on dynamic strength of sandstone are presented in Fig. 13a. It can be concluded that the dynamic strength of sandstone decreases with increasing σ_1 , but increases with the increasing of σ_2 . From the view of mechanics, the initial σ_2 in lateral direction confines the dilation of the cracks propagation and coalescence along the direction of σ_1 during the impact, resulting in an enhancement of rock strength. In addition, it is shown from Fig. 13b that σ_1 and σ_2 also affect the failure strain of sandstone. As the failure occurs at very small strains in sandstone, the obtained failure strains are scattered, and yet indicate that the failure strain decreases slightly with increasing σ_1 and σ_2 in the dynamic biaxial tests.

The evolution of confinement stress in the Y direction can be obtained by strain gauges mounted on the lateral Y bars. It is found that the confining stresses applied on the specimen

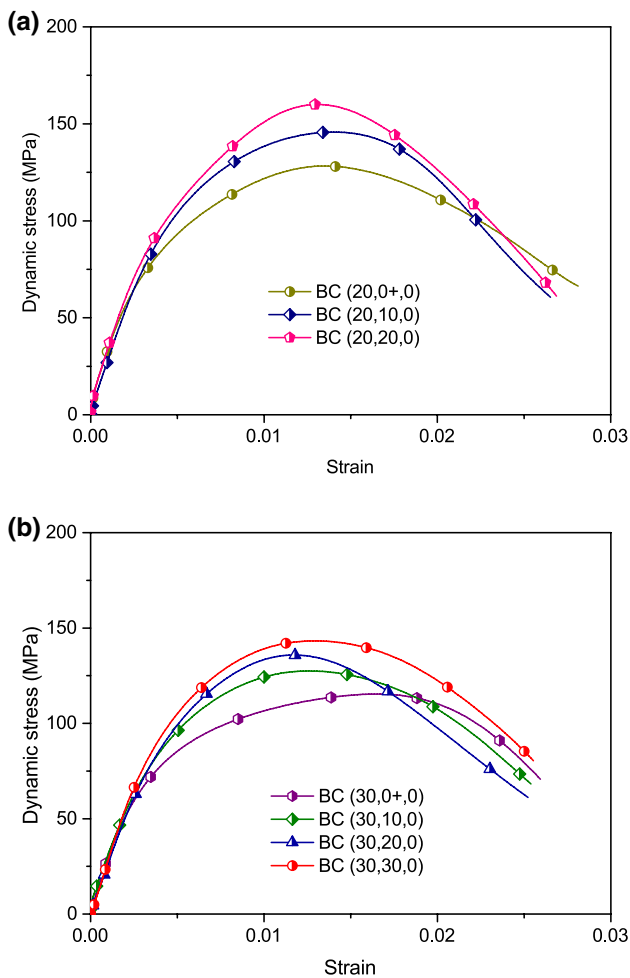


Fig. 12 Effects of intermediate principal pre-stress σ_2 on the dynamic stress–strain curve of sandstone under biaxial compression (BC biaxial compression)

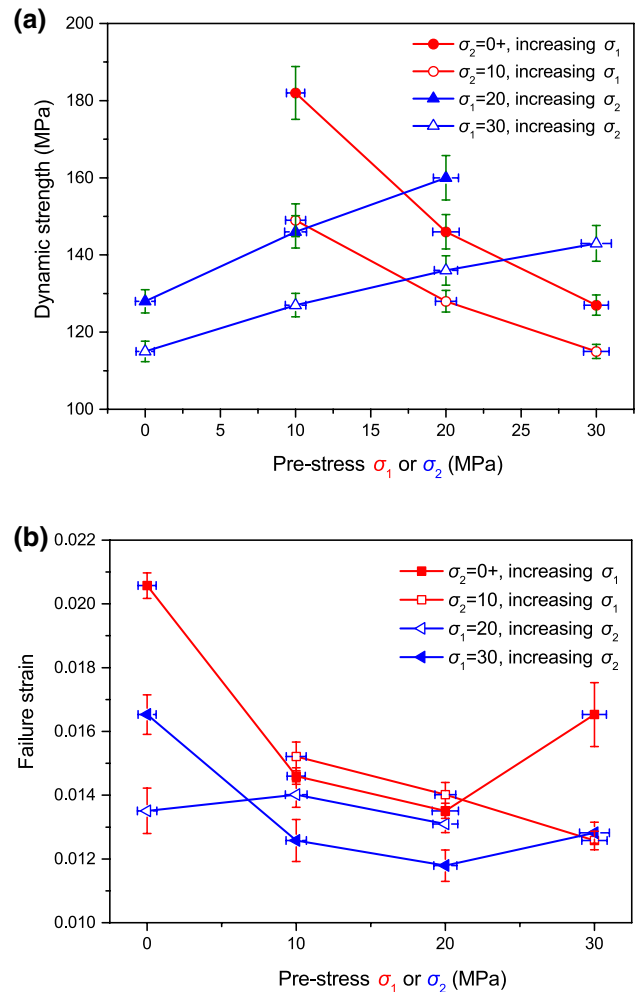


Fig. 13 Effects of σ_1 or σ_2 on **a** dynamic strength, and **b** failure strain of sandstone

along Y direction are not constant during the impact. Under the axial compressive loading from X direction, the rock specimen expands in the lateral direction before the failure. This lateral expansion induces stress wave to propagate along the bar in the Y direction.

The real-time deformation and fracturing process of sandstone are successfully captured using high-speed photography. During a typical impact in biaxial compression, rock ejection phenomenon occurs at the free boundary along the Z direction. As shown in Fig. 14, rock specimen deformed elastically without visible cracks during the first 50 μ s and then obvious vertical strain in Z direction emerged due to the expansion before 150 μ s. Subsequently, a rock slab generated and flew away with an initial velocity from the free surface; it was then broken into two pieces in the air with an obvious tensile crack, which is spalled by the reflected tensile stress wave. Following the flying rock, it is observed that a number of small fragments also ejected out from the

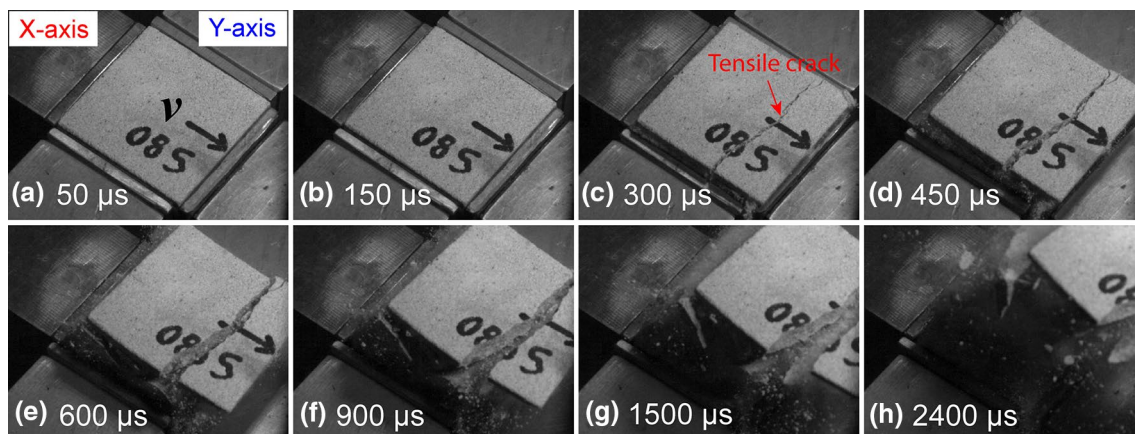


Fig. 14 Rock ejection during biaxial compression with the pre-stress of (20, 20, 0) MPa

specimen around 1500 μ s. The ejection process of sandstone was predominantly slabbing, where a few slabs ejected away from the complete exposed surface of the specimen. This phenomenon represents the rock failure process during a rock burst induced by dynamic disturbances around underground openings (Kaiser and Cai 2012).

Figure 15 shows typical fracture modes of biaxial compression tests. Rocks are broken into fragments with some fracture planes. The direction of the rock fracture is near parallel to σ_1 and perpendicular to σ_3 , which agrees well with the conventional rock mechanics (Jaeger et al. 2009). When the pre-stresses increase from (20, 20, 0) to (30, 30, 0) MPa, the number of macroscopic fracture planes decreases, verifying that the confinement effect plays an important role in fracture behaviour of rocks under biaxial compression.

3.3 Effect of Triaxial Pre-stress

For the dynamic tests with triaxial compression, following the loading path in Fig. 6, rocks are subjected to specified triaxial pre-stress states, including hydrostatic compression ($\sigma_1 = \sigma_2 = \sigma_3 \neq 0$) and true triaxial compression ($\sigma_1 > \sigma_2 > \sigma_3 \neq 0$) states. Subsequently, dynamic loadings are applied by launching the striker bar with an impact velocity of 20 m/s. The effects of σ_1 , σ_2 and σ_3 on dynamic mechanical and fracture behaviour of sandstone are quantified and discussed in detail.

Figure 16 presents the dynamic stress–strain curves of sandstone under different hydrostatic states. The dynamic strength of sandstone increases drastically to over 200 MPa if confinement exists in three directions, compared to that of the dynamic UCS of 93 MPa under the same impact velocity, which verifies that rocks are highly sensitive to the confining stresses. When the initial hydrostatic stress states vary from (0 +, 0 +, 0 +) to (30, 30, 30) MPa by simultaneously increasing σ_1 , σ_2 and σ_3 , the peak strength exhibits an

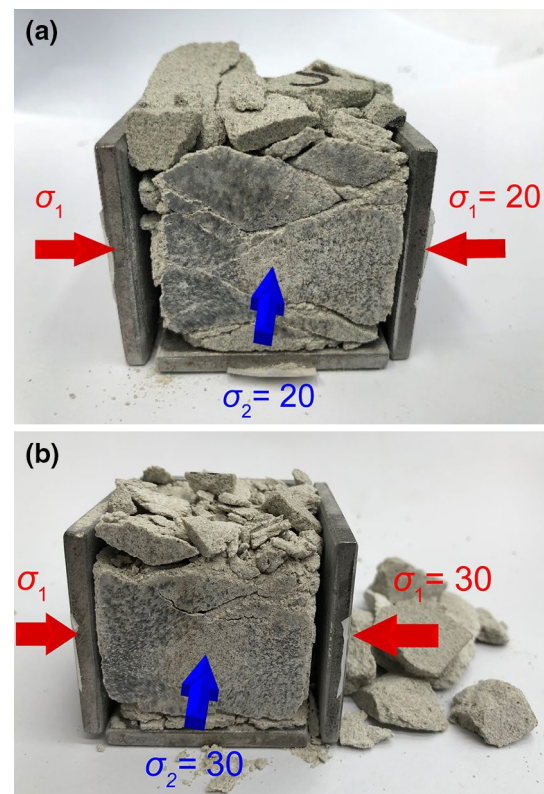


Fig. 15 Failure observation of sandstone in dynamic compression tests with biaxial pre-stresses: **a** (20, 20, 0) MPa; **b** (30, 30, 0) MPa

enhancement from 214 to 246 MPa. On the other side, the peak strain drops dramatically from 0.02 to 0.01, which indicates that rocks can resist high external stress with a smaller deformation at high hydrostatic compression stress states. Besides, rocks under a pre-stress state of (0 +, 0 +, 0 +) MPa are fractured into small pieces with macroscopic fractures after impact. As the initial hydrostatic stress increases to (30, 30, 30) MPa, rocks appear visually intact but with

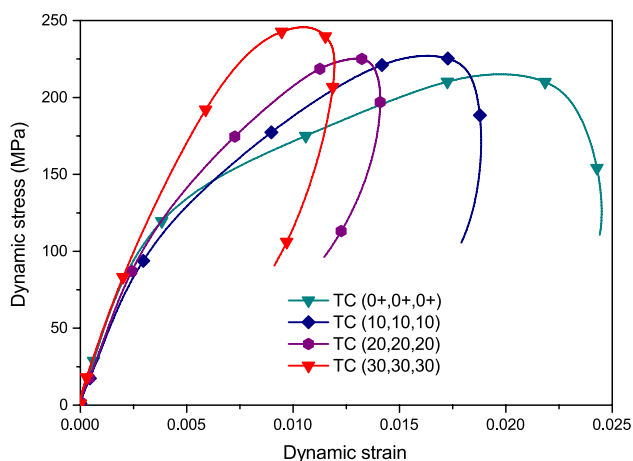


Fig. 16 Dynamic stress–strain curves of sandstone at the impact velocity of 20 m/s under hydrostatic compression (TC triaxial compression)

prevailing micro-cracks, which results in an obvious deformation resilience at the post-peak stage of the stress–strain curve. This result also implies that the residual strength of rock also depends on the value of the confining pre-stresses.

To study the effects of σ_1 on dynamic triaxial strength of rocks, sandstone specimens under the initial stress state of $\sigma_1 > \sigma_2 = \sigma_3$ are impacted, and the experimental results in Fig. 17a show that dynamic triaxial strength of sandstone decreases with the increase of σ_1 varying from (0 +, 0 +, 0 +) to (30, 0 +, 0 +) MPa. Similar results can be obtained in Fig. 17b where rock is confined with the true triaxial pre-stress states changing from (10, 20, 10) to (30, 20, 10) MPa. The mechanism involving the effects of σ_1 on rock strength under dynamic true triaxial tests can be attributed to the induced damage and cracks activated by the pre-stress along impact direction before dynamic loadings, which is similar to that of the dynamic uniaxial and biaxial loads.

In Fig. 17c, d, the effects of σ_2 on the dynamic stress–strain curve are presented (i.e. with approximately the same axial strain rate of 110/s for different tests). It is noteworthy to note here, unlike the effect of σ_1 , the σ_2 not only affects the strength of sandstone but also on the threshold of failure strain. As shown in Fig. 17c, the strength of rock increases from 199 to 222 MPa when the pre-stress states vary from (20, 0 +, 0 +) to (20, 20, 0 +) MPa with increasing σ_2 by 10 MPa. However, the corresponding strain reduces from 0.02 to 0.017 by 15%. Figure 17d illustrates the effect of σ_2 on the dynamic stress–strain curves when the triaxial pre-stress states vary from (30, 0 +, 10) to (30, 30, 10) MPa. With increasing σ_2 from 0 + to 10 MPa, the dynamic strength of sandstone increases considerably from 191 to 215 MPa, but with a significant failure strain reduction from 0.02 to 0.0149, which indicates that σ_2 plays an important role in dynamic properties of rock. Figure 17e shows the

effect of σ_3 on the dynamic stress–strain curve of sandstone under triaxial pre-stress conditions and demonstrates that σ_3 play a role that is similar to that of the σ_2 . That is, an increase of σ_3 increases the dynamic strength but reduces the peak strain. With the increase of σ_3 , the sandstone can withstand a higher load. However, the axial deformation of sandstone specimen is significantly reduced. As shown in Fig. 17f, when the σ_3 increases from 0 + to 30 MPa with constant $\sigma_2 = \sigma_3 = 30$ MPa, the reduction of failure strain becomes smaller as the general triaxial stress state becomes more and more uniform. In the view of mechanics, lateral confinement provided by σ_2 and σ_3 restricts the dilatancy of rock during impact, which contributes to the increase of dynamic strength. Another factor that can cause an increase in rock strength is the dynamic friction of the contact surfaces between the specimen and lateral bars, and grease is used to minimise this effect.

The fractured rock specimens can be classified according to not only testing parameters but also failure modes. Although it is realised that certain features of the fracture mode may be a result from constraints imposed by the testing system, changes in fracture modes are consistent with the values of the three principal pre-stresses. At the same loading conditions, the system constraints on the specimen remained essentially constant. Figure 18a shows typical failure modes of sandstone after impact under dynamic true triaxial compression. Rock specimens appear failure planes parallel to σ_2 , which is expected as theoretically, i.e. rock dilates more towards the lowest stress. It can be found that shear fracture becomes dominant, and varying angles formed fracture planes with respect to the direction of minimum principal stress σ_3 are between 79° and 76° (shown in Fig. 18a). The angle of shear fracture plane depends not only on the three principal pre-stresses (Mogi 1971; Haimson 2012), but also on the impact velocity and rock materials properties such as the cohesion and friction angle. Under the higher pre-stresses state of (30, 20, 20) MPa, sandstone specimens remain intact in shape with mesoscopic damage, such as grain dislocation, crushing and rotation.

3.4 CT Reconstruction of Triaxial Pre-stress

Micro-CT (μ CT) allows analysis of a representative volume with a high resolution down to the microscale and enables the reconstruction of a realistic virtual 3D model of geomaterials. In this study, it is applied to observe non-destructively the deformation and failure characteristics of a tested specimen after triaxial compression. A series of tomographic cross-sections of sandstone specimen under different pre-stress conditions is shown in Fig. 19. The brightness contrasts represent the X-ray attenuation in each material, which depends on the atomic number and the density of the material. Due to different X-ray opacity of rock materials,

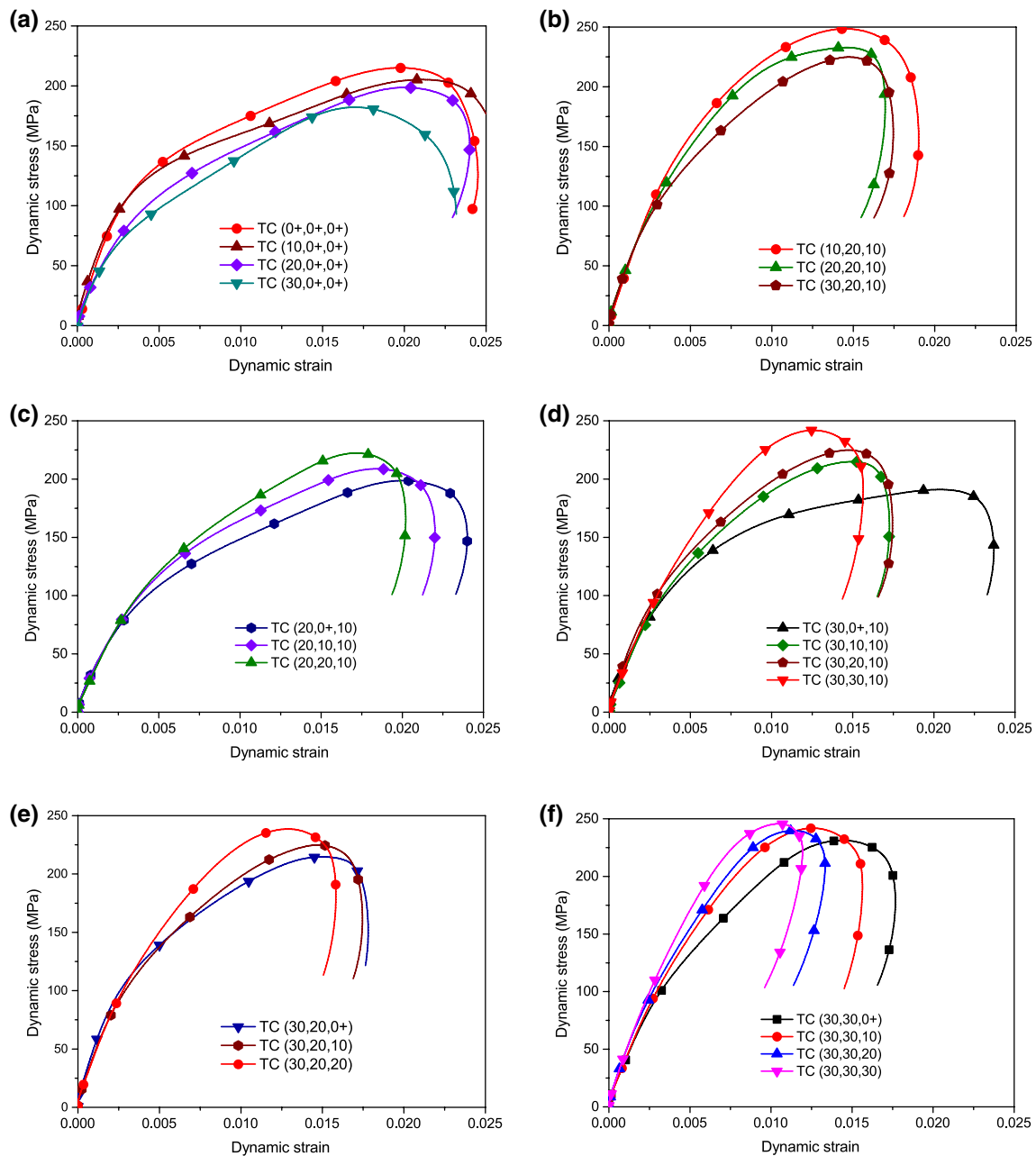


Fig. 17 Dynamic stress–strain curves of sandstone at the impact velocity of 20 m/s under triaxial compression: **a, b** effects of σ_1 ; **c, d** effects of σ_2 ; **e, f** effects of σ_3 (TC triaxial compression)

the high-density areas are the mineral grains shown as white and grey, while the low-density areas are the cracks shown as black lines. For rock specimen with the pre-stress of (10, 0 +, 0 +) MPa. The double ‘V’ type of fracture pattern is clearly observed, which is highly involved in shear failures. The shape and extents (width and depth) of the fracture pattern depend upon the magnitude of applied pre-stresses as well as dynamic stress during impact.

Based on stacks of 2D image slices, the 3D impression of the whole specimen can be visualised by volume

rendering and shown in Fig. 18b. It can be seen that the X-ray CT scanning images approximate the actual crack photographs, which demonstrate that X-ray micro-CT scanning can be used to explore the internal damage of sandstone materials. Image segmentation is always an important process in digital image processing, which aims to extract several parts with similar features or attributes in images stacks. By using a threshold segmentation technique, a proper threshold is set to digitally distinguish cracks from the grains of the sandstone specimen. The 3D

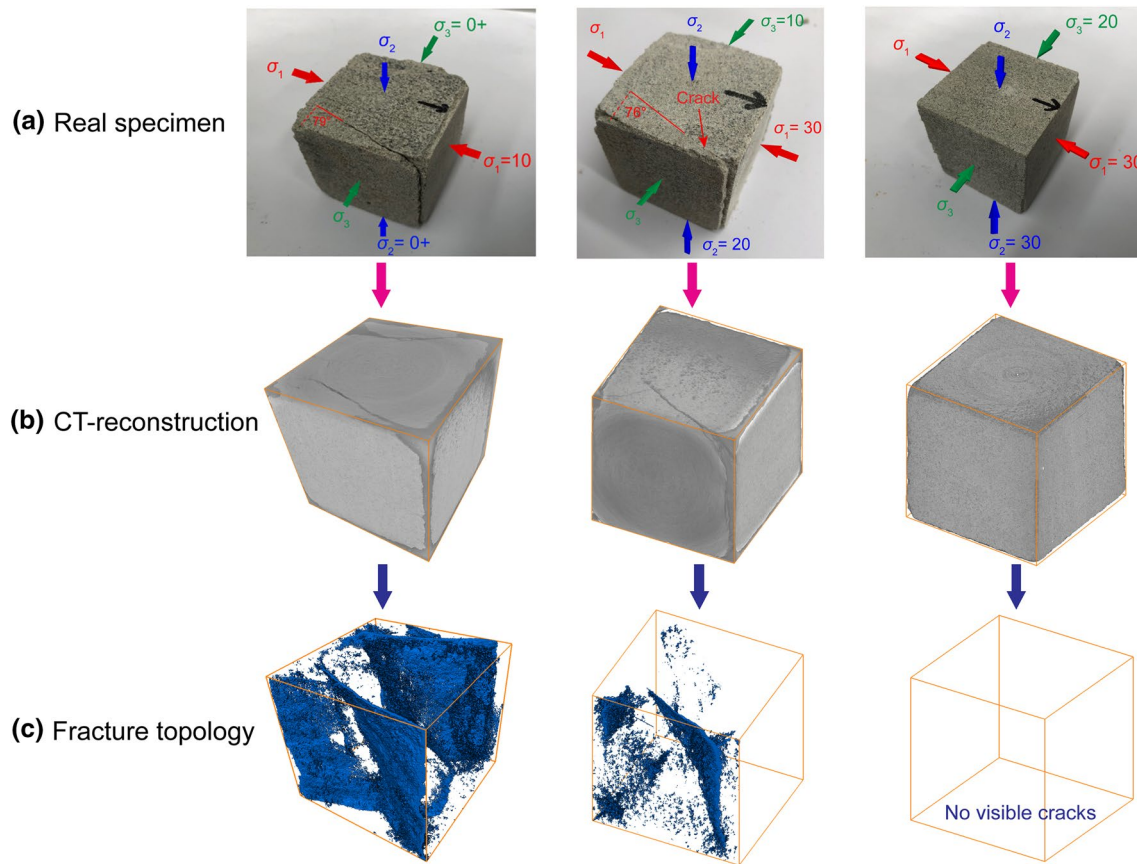


Fig. 18 Tested rock specimens and X-ray micro-CT reconstruction: **a** real sandstone specimen under different pre-stress conditions; **b** volume rendering from CT images; **c** fracture topology

fracture topology inside the specimen was reconstructed vividly and shown in Fig. 18c. Fractures were recognised and transferred to blue pixels, while the remainder is transferred to colourless pixels. For rock specimen under the pre-stress of (30, 20, 10) MPa, it can be seen that two sets of fractures initiate and extend from the surface into the rock. These fractures can cause the ‘V’ type of fracture pattern when they intersect one another. However, in this case, they arrest during propagation and thus the coalescence of crack is not achieved. Under the higher pre-stress state of (30, 20, 20) MPa, there is no visible crack in the whole specimen, which is also verified by tomographic cross-sections shown in Fig. 19c. The fracture pattern of rock specimen changes from fully double ‘V’ type to intact shape without visible cracks when the pre-stresses vary from (10, 0 +, 0 +) to (30, 20, 20) MPa, indicating the confinement dependence of rock.

4 Comparisons and Discussion

It is found that the dynamic strength of sandstone is sensitive to three principal stresses under triaxial pre-compression condition. When lateral confinement was applied on the specimen, the stress–strain behaviour is largely different from that observed in the dynamic uniaxial compression case. Figure 20 demonstrates the dynamic stress–strain curves of sandstone at the impact velocity of 20 m/s under uniaxial, biaxial and triaxial compression tests, and rocks deform at the average strain rate of approximate 110/s. Compared to the dynamic uniaxial unconfined strength (93 MPa) of sandstone, at the impact velocity of 20 m/s, the dynamic triaxial strength increase evidently to around 250 MPa, which verifies that dynamic strength of rocks is confinement dependent. Test results illustrate that the enhancement of rock strength depends on confinement condition under fixed impact velocity. The dynamic strength of sandstone can be classified into three levels (i.e. 50–100 MPa, 100–150 MPa, and 180–250 MPa)

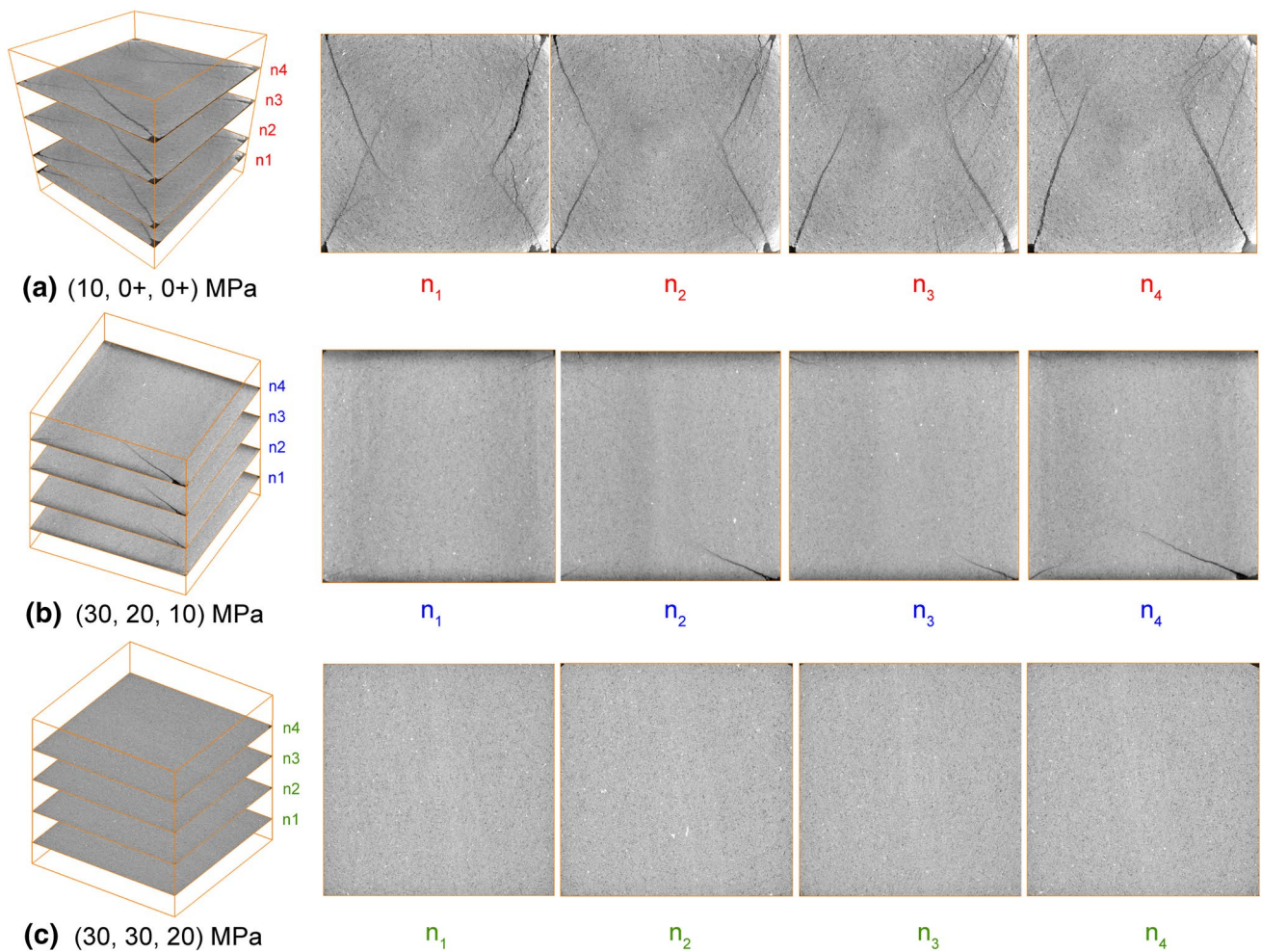
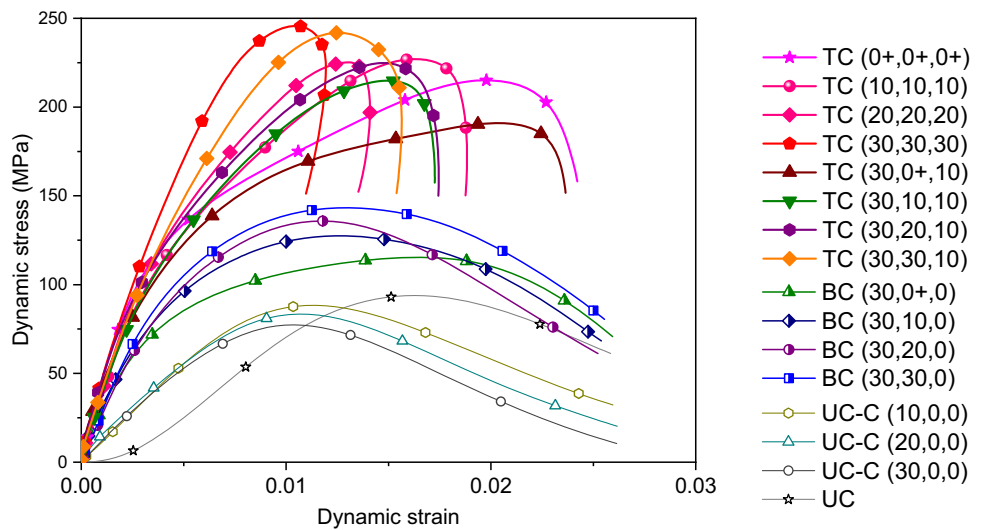


Fig. 19 Tomographic cross-sections of sandstone at the impact velocity of 20 m/s under different pre-stress conditions

Fig. 20 Dynamic stress–strain curves of sandstone at the impact velocity of 20 m/s under uniaxial, biaxial and triaxial compression (UC uniaxial compression, UC-C confined UC, BC biaxial compression, TC triaxial compression)



according to the confinement conditions of uniaxial, biaxial and triaxial compression. The propensity for crack growth can be suppressed by the lateral confinement pressure (Chen and Ravichandran 1997), and thus multi-stress state or lateral confinement contributes to the increase of dynamic strength of rocks.

For all conditions, beginning at zero stress, there exists a distinct linear elastic region of the stress–strain curves. The strain–stress curve obtained from conventional dynamic UC test possesses an initial compaction state, followed by linear elastic deformation and nonlinear damage until failure of rock at the peak strength. As for the deformation behaviour, there is a little deviation of linear elastic deformation before fracture in the dynamic UC test. Moreover, for dynamic confined tests of sandstone, the inelastic strain at maximum stress was of the same order of magnitude with elastic strain. Besides, the fracture behaviour of sandstone is significantly dependent on the confinement condition. In dynamic uniaxial and biaxial compression tests, rocks are impacted into fragments or even in powder, which leads to the post-peak strain continues to increase. However, under the true triaxial compression condition, the predominant failure mode is shear-type failures. Under the high triaxial pre-stress states like hydrostatic pressure confinement, rocks are geometrically intact with some damages such as grain deformation and dislocation. The post-peak strain of rock decreases in the unloading phase with a fast release of stored strain energy, which results in a distinct closed-loop in the post-peak of dynamic stress–strain curves.

The elastic modulus of rock is determined as the slope of the strain–stress history before the nonlinear segments. The average elastic modulus of sandstone are 11, 28 and 36 GPa for uniaxial, biaxial and triaxial compression, respectively, showing a rapid increase with confinement conditions changing from 1D to 3D, which can be obtained in Fig. 20. Theoretically, the elastic modulus is 15.9 GPa which can be calculated by $E = \rho C_L^2$. However, because of the compaction from applied confined stresses, both density ρ and P-wave velocity C_L of rocks increase as the porosity of rocks decreases. In this regard, the initial confinement contributes to the enhancement of rock elastic modulus. Besides, the dynamic evolutions of lateral confining stresses on the rock specimen are also affected by the stiffness of output X and Y bars. Thus the increase of elastic modulus with confinement from 1D to 3D can be a combined material/structure phenomenon.

During the impact of a dynamic true triaxial test, the lateral confining stresses σ_2 and σ_3 applied on the specimen are not constant. Instead, they increase gradually with the axial compressive loading from X direction. The increments $\Delta\sigma_2$ and $\Delta\sigma_3$ depend not only on the impact velocity of striker, but also on the material parameters (e.g. Poisson's ratio, elastic modulus and P-wave velocity) of the tested specimen

and the bars. In the impact direction, the axial pre-stress acting on the specimen is assumed to be constant during the impact because of the delayed feedback of hydraulic cylinder, and thus the σ_1 includes both static pre-stress and dynamic stress. Actually, the total strength of rock is the sum of static pre-stress and dynamic strength. Further investigations of total strength are being conducted to study the effects of confinements and loading rates.

5 Conclusions

Dynamic properties of sandstone under various multiaxial loads including uniaxial, biaxial and triaxial compression were systematically studied using a newly developed triaxial Hopkinson bar system. The real-time deformation characteristics of rock under dynamic biaxial compression were digitally captured using the high-speed camera, and fracture patterns of rocks under dynamic triaxial compression were non-destructively identified by the μ CT system. Under the impact of the same velocity, dynamic properties including compressive failure strength, failure strain, elastic modulus and failure modes were discussed in detail. The main conclusions are as following:

1. The triaxial Hopkinson bar is capable of recreating specified quasi-static stress states on geomaterials and followed by applying dynamic loadings, which allows precise determination of dynamic stress–strain of materials under multiaxial loading conditions. Experiments on sandstone specimens with various combination of static–dynamic loading demonstrate that the new test apparatus is of great robust with reliable data. In the dynamic triaxial tests, due to the Poisson's effect of materials, three principal stresses (σ_1 , σ_2 and σ_3) acting on the rock specimen vary with the input dynamic loads and can be captured successfully by strain gauges on the six bars. The obtained signals provide not only the stress–strain information of materials, but also the stress states at which material damage and fracturing.
2. Dynamic stress–strain curves share a linear region at the beginning of dynamic loading, and the peak strain shows a decreasing trend as the confining stresses increase. Moreover, the elastic modulus increases with confinement conditions varying from uniaxial, biaxial to triaxial compression. Dynamic strength of rocks is also dependent on confinements, and it decreases with the increasing axial pre-stress σ_1 along impact direction, but enhances with the increase of lateral pre-stresses σ_2 and σ_3 . Microcracks inside specimens are reactivated by pre-stress σ_1 , and thus a damage state is induced. However, the dilatancy for crack growth in the σ_1 direction is suppressed by the lateral confining pre-stresses.

3. Failure modes of sandstone also exhibit confinement dependence at the same impact velocity. Rocks can be pulverised into powder in uniaxial compression, and the rock ejection phenomenon occurs from the free surface in dynamic biaxial compression. However, in dynamic triaxial compression, rocks are fractured with a macroscopic shear fracture at low pre-stress states and remain intact in shape with great damage when pre-stresses increase.

Acknowledgements The triaxial Hopkinson bar and high-speed DAQ system were sponsored by Australian Research Council (LE150100058), and the corresponding author was mainly responsible for its development. We would like to thank Dr. Songlin Xu of University of Science and Technology of China and Mr. Xiaoyong Song of Luoyang Liwei Technology Co., Ltd. for helping us develop the triaxial Hopkinson bar. The costs of specimen preparation and CT scanning were supported by Engineering Seed Funding Scheme at Monash University 2018 and National Nature Science Foundation of China (no. 41525009). The first author acknowledges the financial support from Australian International Postgraduate Research Scholarship and Monash Graduate Scholarship.

References

- Ahorner L (1975) Present-day stress field and seismotectonic block movements along major fault zones in Central Europe. *Tectonophysics* 29:233–249
- Akers SA, Reed PA, Ehrig JQ (1986) WES high-pressure uniaxial strain and triaxial shear test equipment. Department of the Army, Waterways Experiment Station, Corps of Engineers, Structures Laboratory
- Al Mahbub A, Haque A (2016) X-ray computed tomography imaging of the microstructure of sand particles subjected to high pressure one-dimensional compression. *Materials* 9(11):890
- Albertini C (2013) Physical principles and feasibility study of a 3D-modified Hopkinson bar for the impact testing in compression of rock specimens at EPFL-LMR. First Phase Report of Contract between SUPSI/Dynalab and Ecole Polytechnique Federale de Lausanne, Laboratoire de Mecanique des Roches
- Albertini C, Montagnani M (1994) Study of the true tensile stress-strain diagram of plain concrete with real size aggregate; need for and design of a large Hopkinson bar bundle. *J Phys IV* 04:C8–C113. <https://doi.org/10.1051/jp4:1994817>
- Bailly P, Delvare F, Vial J, Hanus JL, Biessy M, Picart D (2011) Dynamic behavior of an aggregate material at simultaneous high pressure and strain rate: SHPB triaxial tests. *Int J Impact Eng* 38:73–84. <https://doi.org/10.1016/j.ijimpeng.2010.10.005>
- Barton N, Shen B (2017) Risk of shear failure and extensional failure around over-stressed excavations in brittle rock. *J Rock Mech Geotech Eng* 9:210–225
- Brown E, Hoek E (1978) Trends in relationships between measured in-situ stresses and depth. *Int J Rock Mech Min Sci Geomech Abstr* 4:211–215
- Cadoni E (2010) Dynamic characterization of orthogneiss rock subjected to intermediate and high strain rate in tension. *Rock Mech Rock Eng* 43:667–676
- Cadoni E, Albertini C (2011) Modified Hopkinson bar technologies applied to the high strain rate rock tests. *Advances in rock dynamics and applications*. CRC Press, USA, pp 79–104
- Cadoni E, Cadoni E, Dotta M, Forni D, Riganti G, Albertini C (2015) First application of the 3D-MHB on dynamic compressive behavior of UHPC. *EPJ Web Conf* 94:01031. <https://doi.org/10.1051/epjconf/20159401031>
- Cai M (2008) Influence of intermediate principal stress on rock fracturing and strength near excavation boundaries—insight from numerical modeling. *Int J Rock Mech Min Sci* 45:763–772
- Cai M, Kaiser P, Suorineni F, Su K (2007) A study on the dynamic behavior of the Meuse/Haute-Marne argillite. *Phys Chem Earth Parts A/B/C* 32:907–916
- Chang C, Haimson B (2000) True triaxial strength and deformability of the German Continental Deep Drilling Program (KTB) deep hole amphibolite. *J Geophys Res Solid Earth* 105:18999–19013
- Chen W, Ravichandran G (1996a) An experimental technique for imposing dynamic multiaxial-compression with mechanical confinement. *Exp Mech* 36:155–158
- Chen W, Ravichandran G (1996b) Static and dynamic compressive behavior of aluminum nitride under moderate confinement. *J Am Ceram Soc* 79:579–584
- Chen W, Ravichandran G (1997) Dynamic compressive failure of a glass ceramic under lateral confinement. *J Mech Phys Solids* 45:1303–1328
- Chen W, Song B (2010) Split Hopkinson (Kolsky) bar: design, testing and applications. Springer, Berlin
- Chen R et al (2016) Dynamic fracture properties of rocks subjected to static pre-load using notched semi-circular bend method. *Rock Mech Rock Eng* 49:3865–3872
- Chen R, Yao W, Lu F, Xia K (2017) Evaluation of the stress equilibrium condition in axially constrained triaxial SHPB tests. *Exp Mech* 2017:1–5
- Chester FM, Chester JS (2000) Stress and deformation along wavy frictional faults. *J Geophys Res Solid Earth* 105:23421–23430
- Christensen RJ, Swanson SR, Brown WS (1972) Split-Hopkinson-bar tests on rock under confining pressure. *Exp Mech* 12:508–513. <https://doi.org/10.1007/bf02320747>
- Cnudde V, Boone MN (2013) High-resolution X-ray computed tomography in geosciences: a review of the current technology and applications. *Earth Sci Rev* 123:1–17
- Dai F, Huang S, Xia K, Tan Z (2010) Some fundamental issues in dynamic compression and tension tests of rocks using split Hopkinson pressure bar. *Rock Mech Rock Eng* 43:657–666. <https://doi.org/10.1007/s00603-010-0091-8>
- Descamps F, da Silva MR, Schroeder C, Verbrugge JC, Tshibangu J (2012) Limiting envelopes of a dry porous limestone under true triaxial stress states. *Int J Rock Mech Min Sci* 56:88–99
- Doan ML, Gary G (2009) Rock pulverization at high strain rate near the San Andreas fault. *Nat Geosci* 2:709
- Du K, Tao M, Li XB, Zhou J (2016) Experimental study of slabbing and rockburst induced by true-triaxial unloading and local dynamic disturbance. *Rock Mech Rock Eng* 49:3437–3453
- Engelder T, Sbar ML (1984) Near-surface in situ stress: introduction. *J Geophys Res* 89:9321–9322
- Farbaniec L, Hogan JD, Xie KY, Shaeffer M, Hemker KJ, Ramesh KT (2017) Damage evolution of hot-pressed boron carbide under confined dynamic compression. *Int J Impact Eng* 99:75–84
- Ferrari F, Lavecchia G, de Nardis R, Brozzetti F (2015) Fault geometry and active stress from earthquakes and field geology data analysis: the Colfiorito 1997 and L'Aquila 2009 Cases (Central Italy). *Pure Appl Geophys* 172:1079–1103
- Forquin P, Gary G, Gatuingt F (2008) A testing technique for concrete under confinement at high rates of strain. *Int J Impact Eng* 35:425–446. <https://doi.org/10.1016/j.ijimpeng.2007.04.007>

- Frew D, Forrestal MJ, Chen W (2001) A split Hopkinson pressure bar technique to determine compressive stress–strain data for rock materials. *Exp Mech* 41:40–46
- Frew DJ, Akers SA, Chen W, Green ML (2010) Development of a dynamic triaxial Kolsky bar. *Meas Sci Technol* 21:105704. <https://doi.org/10.1088/0957-0233/21/10/105704>
- Gary G, Bailly P (1998) Behaviour of quasi-brittle material at high strain rate. Experiment and modelling. *Eur J Mech A Solids* 17:403–420
- Gong J, Malvern L (1990) Passively confined tests of axial dynamic compressive strength of concrete. *Exp Mech* 30:55–59
- Green S, Perkins R (1968) Uniaxial compression tests at varying strain rates on three geologic materials. In: The 10th US symposium on rock mechanics (USRMS), American Rock Mechanics Association
- Haimson B (2012) True triaxial testing reveals hitherto unknown rock mechanical properties. *True Triaxial Test Rocks* 4:159
- Hast N (1969) The state of stress in the upper part of the earth's crust. *Tectonophysics* 8:169–211
- He M, e Sousa LR, Miranda T, Zhu G (2015) Rockburst laboratory tests database—application of data mining techniques. *Eng Geol* 185:116–130
- Hokka M et al (2016) Effects of strain rate and confining pressure on the compressive behavior of Kuru granite. *Int J Impact Eng* 91:183–193
- Hopkinson B (1914) A method of measuring the pressure produced in the detonation of high explosives or by the impact of bullets. *Proc Camb Philos Soc* 213:437–456. <https://doi.org/10.1098/rsta.1914.0010>
- Huang R, Wang X (1999) Analysis of dynamic disturbance on rock burst. *Bull Eng Geol Environ* 57:281–284
- Ingraham M, Issen K, Holcomb D (2013) Response of Castlegate sandstone to true triaxial states of stress. *J Geophys Res Solid Earth* 118:536–552
- Jaeger JC, Cook NG, Zimmerman R (2009) *Fundamentals of rock mechanics*. Wiley, Oxford
- Kabir ME, Chen WN (2009) Measurement of specimen dimensions and dynamic pressure in dynamic triaxial experiments. *Rev Sci Instrum* 80:125111. <https://doi.org/10.1063/1.3271538>
- Kaiser PK, Cai M (2012) Design of rock support system under rockburst condition. *J Rock Mech Geotech Eng* 3:215–227
- Karl T, Richart Jr (1952) Stresses in rock about cavities. *Geotechnique* 3:57–90
- Kawakita M (1981) The dynamic fracture properties of rocks under confining pressure. *Mem Fac Eng Hokkaido Univ* 15:467–478
- Kolsky H (1949) An investigation of the mechanical properties of materials at very high rates of loading. *Proc Phys Soc* 62:676
- Kolsky H (1953) *Stress wave in solids*. Clarendon Press, Oxford
- Kumar A (1968) The effect of stress rate and temperature on the strength of basalt and granite. *Geophysics* 33:501–510
- Kwasniewski M, Takahashi M, Li X (2003) Volume changes in sandstone under true triaxial compression conditions. In: 10th ISRM congress. International Society for Rock Mechanics
- Kwaśniewski M (2012) Mechanical behavior of rocks under true triaxial compression conditions—a review. *True Triaxial Test Rocks* 4:99
- Lankford J (1976) *Dynamic strength of oil shale, vol 16*
- Lankford J (1994) Utilization of the split Hopkinson pressure bar under hydrostatic confining pressure to characterize the compressive behavior of ceramics and ceramic composites. *ASME Appl Mech Div Publ* 197:1
- Lee FT, Abel JF Jr, Nichols TC Jr (1976) The relation of geology to stress changes caused by underground excavation in crystalline rocks at Idaho Springs, Colorado. US Govt. Print. Off
- Lee H, Haimson BC (2011) True triaxial strength, deformability, and brittle failure of granodiorite from the San Andreas Fault Observatory at Depth. *Int J Rock Mech Min Sci* 48:1199–1207
- Li XB, Lok T, Zhao J (2005) Dynamic characteristics of granite subjected to intermediate loading rate. *Rock Mech Rock Eng* 38:21–39
- Li XB, Zhou ZL, Lok T-S, Hong L, Yin T (2008) Innovative testing technique of rock subjected to coupled static and dynamic loads. *Int J Rock Mech Min Sci* 45:739–748. <https://doi.org/10.1016/j.ijrmms.2007.08.013>
- Li XB, Zhou ZL, Zhao FJ, Zuo YJ, Ma CD, Ye ZY, Hong L (2009) Mechanical properties of rock under coupled static–dynamic loads. *J Rock Mech Geotech Eng* 1:41–47
- Li XB et al (2017) Failure mechanism and coupled static–dynamic loading theory in deep hard rock mining: a review. *J Rock Mech Geotech Eng* 9:767–782
- Lindholm US (2012) *Mechanical behavior of materials under dynamic loads: symposium held in San Antonio, Texas, September 6–8, 1967*. Springer, Berlin
- Lindholm US, Yeakley LM, Nagy A (1972) A study of the dynamic strength and fracture properties of rock. Southwest Research Institute, San Antonio
- Lindholm U, Yeakley L, Nagy A (1974) The dynamic strength and fracture properties of dresser basalt. *Int J Rock Mech Min Sci Geomech Abstr* 5:181–191
- Liu K, Zhang QB, Zhao J (2018) Dynamic increase factors of rock strength. *Rock dynamics: experiments, theories and applications: proceedings of the 3rd international conference on rock dynamics and applications (RocDyn-3)*. CRC Press, p 169
- Malvern LE, Jenkins D (1990) Dynamic testing of laterally confined concrete. DTIC Document
- Malvern LE, Ross C (1986) *Dynamic response of concrete and concrete structures*. Florida Univ Gainesville, Dept of Engineering Sciences, Florida
- Martin B, Kabir ME, Chen WN (2013) Undrained high-pressure and high strain-rate response of dry sand under triaxial loading. *Int J Impact Eng* 54:51–63
- McGarr A, Gay N (1978) State of stress in the earth's crust. *Annu Rev Earth Planet Sci* 6:405–436
- Mogi K (1971) Fracture and flow of rocks under high triaxial compression. *J Geophys Res* 76:1255–1269
- Mudau A, Govender R, Stacey T (2016) A step towards combating rockburst damage by using sacrificial support. *J South Afr Inst Min Metall* 116:1065–1074
- Nemat-Nasser, Isaacs J, Rome J (2000) *Triaxial Hopkinson techniques*. ASM International, Materials Park
- Olsson W (1991) The compressive strength of tuff as a function of strain rate from 10^{-6} to $10^3/s$. *Int J Rock Mech Min Sci Geomech Abstr* 1:115–118
- Paliwal B, Ramesh KT, McCauley JW, Chen M (2008) Dynamic compressive failure of AlON under controlled planar confinement. *J Am Ceram Soc* 91:3619–3629
- Paterson MS, Wong T-F (2005) *Experimental rock deformation: the brittle field, 2nd edn*. Springer, Berlin
- Perkins R, Green S, Friedman M (1970) Uniaxial stress behavior of porphyritic tonalite at strain rates to $10^3/s$. *Int J Rock Mech Min Sci Geomech Abstr* 5:527IN5529–5528IN6535
- Read R (2004) 20 years of excavation response studies at AECL's Underground Research Laboratory. *Int J Rock Mech Min Sci* 41:1251–1275
- Rome J, Isaacs J, Nemat-Nasser S (2000) Hopkinson techniques for dynamic triaxial compression tests. *Recent Adv Exp Mech*. <https://doi.org/10.1361/asmhba0003301>
- Schwartzkopf AK, Priest S, Melkoumian N et al (2013) Design and fabrication of a low cost true triaxial cell for testing multiple size specimens[J]. *True Triaxial Test Rocks* 2013:83–93
- Seager J (1964) Pre-mining lateral pressures. *Int J Rock Mech Min Sci Geomech Abstr* 3:413–419

- Takahashi M, Koide H (1989) Effect of the intermediate principal stress on strength and deformation behavior of sedimentary rocks at the depth shallower than 2000 m. In: ISRM international symposium. International Society for Rock Mechanics
- Wang S, Liu KX (2011) Experimental research on dynamic mechanical properties of PZT ceramic under hydrostatic pressure. *Mater Sci Eng A* 528:6463–6468. <https://doi.org/10.1016/j.msea.2011.05.019>
- Wang L, Yu YL (1992) Study on dynamic characteristic of rocks using triaxial. *SHPB Chin J Geotech Eng* 14:76–79
- Wu BB, Chen R, Xia KW (2015) Dynamic tensile failure of rocks under static pre-tension. *Int J Rock Mech Min Sci* 80:12–18
- Wu BB, Yao W, Xia KW (2016) An experimental study of dynamic tensile failure of rocks subjected to hydrostatic confinement. *Rock Mech Rock Eng* 49:3855–3864
- Xia KW, Yao W (2015) Dynamic rock tests using split Hopkinson (Kolsky) bar system—a review. *J Rock Mech Geotech Eng* 7:27–59
- Xia KW, Nasser M, Mohanty B, Lu F, Chen R, Luo S (2008) Effects of microstructures on dynamic compression of Barre granite. *Int J Rock Mech Min Sci* 45:879–887
- Xing HZ, Zhang QB, Braithwaite CH, Pan B, Zhao J (2017) High-speed photography and digital optical measurement techniques in geomaterials: fundamental and applications. *Rock Mech Rock Eng* 50(6):1611–1659
- Xing HZ, Zhang QB, Ruan D, Dehkhoda S, Lu GX, Zhao J (2018a) Full-field measurement and fracture characterisations of rocks under dynamic loads using high-speed three-dimensional digital image correlation. *Int J Impact Eng* 113:61–72
- Xing HZ, Zhang QB, Zhao J (2018b) Stress thresholds of crack development and Poisson's ratio of rock material at high strain rate. *Rock Mech Rock Eng* 51(3):945–951
- Yin ZQ, Li XB, Jin JF, He XQ, Du K (2012) Failure characteristics of high stress rock induced by impact disturbance under confining pressure unloading. *Trans Nonferrous Metals Soc China* 22:175–184. [https://doi.org/10.1016/s1003-6326\(11\)61158-8](https://doi.org/10.1016/s1003-6326(11)61158-8)
- Yuan FP, Prakash V, Tullis T (2011) Origin of pulverized rocks during earthquake fault rupture. *J Geophys Res.* <https://doi.org/10.1029/2010jb007721>
- Zhang QB, Zhao J (2013) Determination of mechanical properties and full-field strain measurements of rock material under dynamic loads. *Int J Rock Mech Min Sci* 60:423–439. <https://doi.org/10.1016/j.ijrmms.2013.01.005>
- Zhang QB, Zhao J (2014) A review of dynamic experimental techniques and mechanical behaviour of rock materials. *Rock Mech Rock Eng* 47:1411–1478. <https://doi.org/10.1007/s00603-013-0463-y>
- Zhao J, Cadoni E (2011) Triaxially compressed Hopkinson bar (TriHB) for geomaterial and construction material testing. The Swiss National Science Foundation (SNSF), R'EQUIP Scheme: 206021_128734 <http://p3.snf.ch/project-128734>
- Zhao J, Zhou YX, Hefny AM, Cai JG, Chen SG et al (1999) Rock dynamics research related to cavern development for ammunition storage. *Tunn Undergr Sp Technol* 14:513–526
- Zhao J, Ranjith PG, Khalili N, Dyskin AV, Liyanapathirana S, Williams DJ, Einav I, Karakus M, Sanjayan JG, Shen L, Ma G, Wu C, Xu C, Scheuermann A, Pasternak E, Leo CJ, Zhao GF, Perera S (2015) Three dimensionally compressed and monitored Hopkinson bar. Australian Research Council (ARC), Linkage Infrastructure, Australian, LE150100058
- Zhou ZL, Li XB, Ye ZY, Liu KW (2010) Obtaining constitutive relationship for rate-dependent rock in SHPB tests. *Rock Mech Rock Eng* 43:697–706. <https://doi.org/10.1007/s00603-010-0096-3>
- Zhou YX, Xia K, Li XB, Li HB, Ma GW, Zhao J et al (2012) Suggested methods for determining the dynamic strength parameters and mode-I fracture toughness of rock materials. *Int J Rock Mech Min Sci* 49:105–112
- Zhou ZL, Li XB, Zou Y et al (2014) Dynamic Brazilian tests of granite under coupled static and dynamic loads. *Rock Mech Rock Eng* 47:495–505

Publisher's Note Springer Nature remains neutral with regard to jurisdictional claims in published maps and institutional affiliations.